

**Electrical characterization and investigation of the
piezoresistive effect of PEDOT:PSS thin films**

A Thesis
Presented to
The Academic Faculty

by

Thomas M. Schweizer

In Partial Fulfillment
of the Requirements for the Degree
Master of Science in the
School of Electrical and Computer Engineering

Georgia Institute of Technology
April 2005

Electrical characterization and investigation of the piezoresistive effect of PEDOT:PSS thin films

Approved by:

Dr. Oliver Brand, Advisor
School of Electrical and Computer Engineering
Georgia Institute of Technology

Dr. Bernard Kippelen
School of Electrical and Computer Engineering
Georgia Institute of Technology

Dr. Mark G. Allen
School of Electrical and Computer Engineering
Georgia Institute of Technology

Date Approved: 15 April 2005

*The greatest obstacle to discovery is not ignorance -
it is the illusion of knowledge.*

Daniel J. Boorstin

ACKNOWLEDGEMENTS

I would like to thank my advisor Dr. Oliver Brand for his support and encouragement. He provided ideas, material, coffee and the good atmosphere that made working in his group worth while. I would also like to thank the committee members, Dr. Bernard Kippelen and Dr. Mark G. Allen for their help and especially for granting access to their labs and equipment. I want to acknowledge my colleagues Kianoush Naeli and Jae Hyeong Seo for their assistance in the cleanroom, with measurement devices and for useful discussions. Many fellow students, staff members and friends helped me during my work and I want to say 'Thank you!' to all of them: Benoit Domercq, Andreas Haldi, Xiaohong Zhang, William Potscavage, Seunghyup Yoo and especially Joshua N. Haddock for sample preparation, Yoonsu Choi for laser mask fabrication and coatings, Farhana Zaman for helping with Labview, Laura Rowe for the SEM pictures, Pezhman Monajemi for the EDX analysis, Janet Cobb for training on the Wyko profilometer, Brent Nelson for taking the IR-images, Andrew Cannon for laser cutting and discussions. Also thanks to Linda Newton for her help with supplies, Anthony Francisco from H.C.Starck for providing Baytron[®] P and Kellie J. Schmitt from DuPont for providing Kapton[®] sheets and material data. Special thanks to Wiebke Hahl for proof-reading and everything else.

TABLE OF CONTENTS

ACKNOWLEDGEMENTS	iv
LIST OF TABLES	vii
LIST OF FIGURES	viii
LIST OF SYMBOLS OR ABBREVIATIONS	x
SUMMARY	xii
I INTRODUCTION	1
1.1 Organic electronics	2
1.1.1 Advantages and drawbacks	3
1.1.2 Fabrication technologies	5
1.1.3 Sensor applications	7
1.2 Charge transport in conductive and semiconductive polymers	8
1.3 Materials	12
1.3.1 Classification by molecular weight	12
1.3.2 Classification by structure	14
1.3.3 PEDOT:PSS	15
1.4 Piezoresistivity	17
1.4.1 General description of the piezoresistive effect	17
1.4.2 Geometrical effect	19
1.4.3 Effective change of resistance due to load	21
1.4.4 State of the art for piezoresistive sensors	21
II SAMPLE PREPARATION	26
2.1 Substrate material	26
2.2 Cleaning procedure	29
2.3 Preparation of PEDOT:PSS resistors	29
2.4 Physical device characterization	30
III CHARACTERIZATION	33
3.1 Film resistance without mechanical stress	33
3.2 Film resistance under mechanical load	35

3.3	Environmental influences	37
3.4	Joule heating	41
3.5	Temperature dependencies	45
3.5.1	Charge transport in PEDOT:PSS	45
3.5.2	Thermal impact on substrate material	50
3.5.3	Thermally activated de-doping	53
3.6	Piezoresistivity found in PEDOT:PSS	54
3.7	Migration of silver ions in PEDOT:PSS	64
IV	CONCLUSIONS AND OUTLOOK	67
4.1	Piezoresistivity found in PEDOT:PSS	67
4.2	Further investigations	68
4.3	General considerations	70
	REFERENCES	71

LIST OF TABLES

Table 1	Denotation of the contractive notation used for the piezoresistive coefficient π . . .	18
Table 2	Gage factor and piezoresistive component α_p for selected metals.	22
Table 3	Maximal piezoresistive coefficients for doped single-crystal silicon.	23
Table 4	Parameters for curve fit of thickness as a function of spin speed for PEDOT:PSS films.	32
Table 5	Parameters for empirical model of mobility following an Arrhenius function for Baytron [®] P.	49
Table 6	Measured change in resistance of a thin film resistor from Baytron [®] P split by origin for different temperatures.	59

LIST OF FIGURES

Figure 1	Conductivity of different materials.	3
Figure 2	Sketch of an ethylene molecule.	8
Figure 3	Sketch of an acetylene molecule.	9
Figure 4	Doping process of polyacetylene with iodine.	10
Figure 5	Mixing of degenerated p-orbitals leading to a band-like structure.	11
Figure 6	Chemical structure of selected conjugated polymers.	12
Figure 7	Chemical structure of selected electro-active oligomers and small molecules. . .	13
Figure 8	Schematic diagram depicting the classes of organic semiconducting materials. .	14
Figure 9	Structure of PEDOT doped with PSS.	15
Figure 10	Piezoresistor under longitudinal and transverse stress.	19
Figure 11	Examples for metal strain gages.	22
Figure 12	Piezoresistor made from a polymer with conductive filler.	24
Figure 13	Device structure for PEDOT:PSS resistors.	27
Figure 14	Stress-strain relationship of Kapton® 500 HN polyimide foil.	27
Figure 15	Surface roughness of a microscope glass slide (50x magnification).	28
Figure 16	Surface roughness of Kapton® 500 HN front side (50x magnification).	28
Figure 17	Photograph of some fabricated samples.	30
Figure 18	Layer thickness of PEDOT:PSS spin-coated on glass.	31
Figure 19	Measured resistance of Baytron® P on glass and on Kapton® as a function of the resistor length.	34
Figure 20	Photograph of measurement fixture with a sample to measure the transverse piezo-resistive effect.	35
Figure 21	Typical measurement curve for changing load on a PEDOT:PSS thin film resistor. .	37
Figure 22	Change in resistance as a function of the applied load.	38
Figure 23	Effect of ambient conditions on resistance of PEDOT:PSS.	39
Figure 24	Effect of ambient conditions on noise in PEDOT:PSS resistors.	40
Figure 25	IR-image of temperature distribution in a self-heated PEDOT:PSS resistor sample. .	42
Figure 26	Peak temperature of a Joule heated sample measured with an IR-camera.	42
Figure 27	Absolute current through sample at different measurement voltages indicating Joule heating effect.	44

Figure 28	Relative current change through sample at different measurement voltages indicating Joule heating effect.	44
Figure 29	Selected data of current and resistance plotted as a function of voltage for different temperatures.	45
Figure 30	Thermal dependence of a resistor made with Baytron [®] P according to the Gaussian Disorder Model.	47
Figure 31	Thermal dependence of a resistor made with Baytron [®] P following an Arrhenius function.	48
Figure 32	Thermal dependence of a resistor made with Baytron [®] P VP AI 4083.	50
Figure 33	Elastic modulus E of Kapton [®] 500 HN as a function of temperature.	51
Figure 34	Drift in measured resistance value caused by creep of the Kapton [®] substrate. . .	52
Figure 35	Current measurements from a thermal runaway process due to decrease in resistance with rising temperature.	55
Figure 36	Experimental temperature values determined from measurements at different voltage as function of the dissipated power.	58
Figure 37	Longitudinal piezoresistive coefficient π_l for Baytron [®] P as a function of temperature.	61
Figure 38	Transverse piezoresistive coefficient π_t for Baytron [®] P as a function of temperature.	61
Figure 39	Longitudinal piezoresistive coefficient π_l for Baytron [®] P VP AI 4083 as a function of temperature.	62
Figure 40	Transverse piezoresistive coefficient π_t for Baytron [®] P VP AI 4083 as a function of temperature.	62
Figure 41	Longitudinal piezoresistive coefficient π_l for 'fused' samples from Baytron [®] P as a function of applied voltage.	64
Figure 42	Microscope image of migrated silver on PEDOT:PSS resistor.	65
Figure 43	SEM picture of grown silver features on PEDOT:PSS resistor.	65
Figure 44	Device structures for Pentacene OFETs.	69

LIST OF SYMBOLS OR ABBREVIATIONS

6T	Hexithiophene, an oligomer consisting of six thiophene rings.
AFM	Atomic force microscopy.
Alq3	Tris(8-quinolinolato)aluminum(III), an organometallic small molecule.
CCD	Charge-coupled device, often used in an array in combination with e.g. photo-diodes as imaging chip.
CMOS	Complementary metal-oxide-semiconductor.
EDX	Energy dispersive x-ray (analysis).
GDM	Gaussian disorder model.
HOMO	Highest occupied molecular orbitals.
LUMO	Lowest unoccupied molecular orbitals.
MDNVB-TEO	Block copolymer made from 2,5-dimethoxy-1,4-di(a-(2-naphthalene vinylene)benzene) and tri(ethylene oxide).
MEMS	Micro electromechanical system(s).
MOSFET	Metal-oxide-semiconductor field-effect transistor.
MWNT	Multi-walled carbon nanotubes.
N3	Abbreviation of an organometallic dye (Ru(4,4'-dicarboxy-2,2'-bipyridine) ₂ cis(NCS) ₂).
OFET	Organic field effect transistor.
OLED	Organic light emitting diode.
PEDOT	Poly(3,4-ethylenedioxythiophene), a conjugated polymer.
PMMA	Poly(methylmethacrylate), a common polymer.
PPy	Polypyrrole, a conjugated polymer.
PSS	Poly(4-styrenesulfonate), a polymer used as dopant for PEDOT.
PVDF	poly(vinylidene fluoride), a piezoelectric polymer.
PVK	Poly(vinylcarbazole), a conjugated polymer.
RH	Relative humidity.
rpm	Revolutions per minute, a unit of angular frequency.

SCFH	Standard cubic feet per hour, a unit of volumetric flow.
SCLC	Space charge limited conduction.
SEM	Scanning electron microscope.
ST638	4,4',4''-Tris(N- (1- naphthyl)-N-phenyl-amino)-triphenylamine, tradename of a small molecule used as dopant.
TNF	Trinitrofluorenone, a small molecule used as electron acceptor.
WORM	Write once - read many times, a special kind of electronic memory.

SUMMARY

The field of organic electronics is recently emerging in modern electrical applications. Organic light emitting diodes have been developed and are implemented in commercially available products. The novel materials are also used in sensor applications, utilizing their intrinsic physical, chemical and electrical characteristics. Poly(3, 4-ethylenedioxythiophene): poly(styrene sulfonic acid) (PEDOT:PSS) is one of the most successful organic conductive materials. Developed for antistatic coatings, it is now used in other fields as well, such as in electro-optical devices as transparent electrodes. One of the reasons for its widely spread use is that water-based dispersions of high quality are available. In addition, it is considered highly stable, resisting degradation under typical ambient conditions. For this work, the usability of PEDOT:PSS as active layer for electromechanical sensor applications was investigated. The electrical properties of the material were characterized including temperature dependencies and environmental influences. A piezoresistive effect with negative sign was found. It is small in magnitude and of the same order as the change in resistance due to geometrical effects. The piezoresistive effect is temperature dependent and increasing in magnitude with higher temperatures. An average longitudinal piezoresistive coefficient π_l of $-5.6 \cdot 10^{-10} \text{ Pa}^{-1}$ at room temperature has been evaluated. The transverse effect under the same conditions is opposite in sign and two thirds in magnitude of the lateral effect. The hole mobility of PEDOT:PSS follows an Arrhenius function and thus the resistivity has a negative temperature coefficient. Some other thermally induced effects have been observed such as de-doping of the material resulting in an irreversibly increased resistivity. Due to the low thermal conductivity of the substrate material used, Joule heating of the samples played an important role during the characterization and was utilized to investigate the temperature dependencies. The change of resistance caused by an applied stress to the sample is small, with a gage factor smaller than one. Other approaches using polymeric materials as sensing layer combinable with the processing technologies for organic electronics are summarized and further investigations are addressed.

CHAPTER I

INTRODUCTION

Sensors enable electronic devices to interact with our physical world. Therefore, non-electrical signals are converted into the electrical domain utilizing transducer effects. Many coupling mechanisms are known and used to transform signals from the physical, biological and chemical domain into electrical variables such as voltage, current, resistance or capacity. Non-electrical signals can be converted to the electrical domain directly, for example when incident light is changing the resistance of a photoresistor through the creation of charge carriers (electron-hole pairs) by the photo effect. There can also be more than one step involved for signal conversion into the electrical world. To go along with the previous example, long wavelength infrared-radiation can also cause a thermally insulated sensor area with a resistor to heat up. Due to the dependence of conductivity on temperature its resistance would change. Thus, the signal is first transformed from radiation to heat and then into the electrical domain.

For microsensor applications, one of the most commonly used transducer effects is the piezoresistive effect converting mechanical stress or strain into a resistance change. Because this effect is high in magnitude for doped single-crystal silicon, this material is used in many sensor applications and has proven success in the field. As a matter of fact, the development of fabrication technologies for micro electromechanical structures (MEMS) was initiated by the desire to build sensors with thin membranes and diffused piezoresistors [1]. Many successful devices, especially silicon pressure sensors, exploit this approach [2]. In other designs, the piezoresistors are used to sense the deflection of silicon cantilevers. To build a sensor for acceleration for example, a mass can be added at the tip of such a beam structure. According to Newton's second law, an acceleration will result in a force acting on that proof mass and the cantilever will deflect. Other devices are operated in a resonant mode. There, a cantilever is excited to vibrate at its characteristic frequency. Small mass changes of the beam can be detected since they will alter the resonance frequency. Such structures are often used for chemical sensing to measure the concentration of specific species. To do so,

the resonant beam is covered with a sensitive layer that will absorb the analyte and thus increase in weight and cause a frequency shift [3]. One of the advantages of piezoresistive sensors made from silicon is the possibility that the mechanical structures can be integrated with the read-out and signal-conditioning circuitry on the same chip.

Although silicon, both as single-crystal and amorphous film, is successfully used for millions of sensors, there are applications where its use is disadvantageous. First of all there are limitations caused by the mechanical properties of silicon. By its crystal nature it is a brittle material and easily breaks when overloaded. Another limitation is given from the processing technologies used to fabricate silicon based sensors. Particularly the need for high temperature process steps to e.g. dope the silicon constricts the assortment of applications. Flexible substrates made out of polymers cannot be used because the plastic material will decompose at high temperatures. Last but not least, silicon has a very high Young's modulus, and to achieve large deflections the mechanical structures have to become very thin which is more difficult to produce.

As for all commercial products, the price usually judges over success or failure. Therefore, cheaper ways to produce a device are always welcome. One division within engineering science with potential for low cost is the relatively new field of organic electronics. Intrinsically conductive and semiconductive organic materials are utilized as functional layers to built electronic circuits. Together with the novel materials comes a new set of processing technologies to apply thin films and for patterning. This new field is interesting for building sensors with different properties and for anticipated lower cost compared to the standard technologies. Thus, it is worthwhile to investigate if these new materials exhibit transducer effects and if theses effects can be utilized to built new, all-plastic sensors.

1.1 Organic electronics

During the last years, much attention has been paid to the filed of organic electronics. Electrical devices made out of plastic materials promise advantages due to their special chemical and electrical behavior compared to standard semiconductors. Organic light emitting diodes (OLEDs), plastic solar cells or organic field effect transistors (OFETs) are only some of the new devices in this area. Great progress has been made to investigate, understand, improve and utilize their unique physical

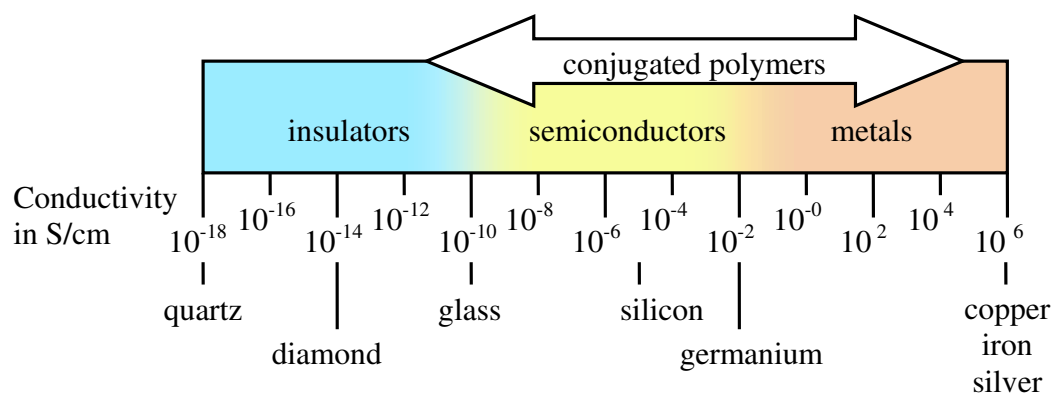


Figure 1: Conductivity of different materials, adapted from [8].

features. Commercial products are entering the consumer markets and show the potential of this new technology.

The foundation of the field of organic electronics was established back in the seventies with the discovery that the conductivity of polyacetylene films can be changed over several orders of magnitude by chemical doping [4]. For their groundbreaking work in this area, MacDiarmid, Heeger and Shirakawa were awarded the Nobel Prize in Chemistry 2000. Excellent introductions into the field of organic electronics are their Nobel lectures [5, 6, 7]. Intrinsic conducting plastic materials and semiconductors, both electron (n-type) and hole transport (p-type) materials with band-like structures, could now be made. Since the early work, many innovative materials in pure form have been developed and characterized for the usage in electronic applications. An overview of the conductivity of different materials from insulators to metals and the span organic materials cover is shown in Figure 1.

1.1.1 Advantages and drawbacks

Organic materials in general possess some unique features. Their chemical structure can be altered and adapted to the need of the application. Especially polymers have advanced far since their first appearance in the early nineteen hundreds [9]. The success of thermoplastics as a cheap and enduring material used widely in our daily life is only but one example. There, the material was designed to be moldable to simplify fabrication but also to exhibit good mechanical characteristics and chemical stability. By changing part of the molecular structure, the behavior of the matter

can be modified. Adding polar *OH* side groups to a molecule will result in a better solubility in water for example. The same approach can be used to adjust the properties of organic electronic material. For instance, an NH_2 group will function as a donor while an NO_2 group will accept electrons in organic nonlinear optical chromophores [10]. The common technologies and techniques to modify the chemical structure can now be applied to adjust the electrical behavior of molecules out of this new class of organic electronic materials. Because there are an almost infinite number of combinations available, the possibilities seem to be virtually unlimited. This is an advantage of organic electronics over the established microelectronic technology. When inorganic single-crystals are used, the electrical properties are changed only by doping. The substrate material itself remains unchanged. Some examples where the versatility of organic electronic materials is used can be given out of the field of optoelectronics. For a full color display, the pixels have to emit light at different wavelengths for red, green and blue. Materials for OLEDs have been developed for all three colors and can even be stacked on each other to achieve a higher pixel density [11, 12]. This approach is more efficient than to use color filters combined with a white light source [13]. Another way to build a true color display utilizing the special features of organic materials is to use a blue or ultraviolet light emitting diode to pump organic fluorescent wavelength down-converters, also known as color-changing media [12]. These materials absorb photons at a short wavelength and emit the energy from a lower bandgap transition at a different color. On the one hand, plenty of opportunities for optimization arise by employing organic materials. On the other hand, an enormous workload has to be covered to investigate which structures and formulas work best.

In the field of optoelectronics, not only the active, emissive layers are of organic origin but also the electrodes by using intrinsic conducting polymers. Organic conductors, distinguishing them from metals, can exhibit high conductivity but still remain transparent. This is due to the low carrier concentration found in most organic materials [5]. Accordingly, they can be used in light emitting diodes or in organic solar cells. The organic materials used as electrodes and the active layers are both pliable. Because plastics can be used as substrate material, the combination provides an opportunity to build flexible devices, something that was not possible with silicon based technology. The realization of ideas such as rollable books and photoelectric cells as plastic sheets becomes more and more likely.

The bases for the novel materials are known components in organic chemistry. This makes them potentially low cost, at least if the fabrication process is not too affording and the material can be mass-produced. Since the materials are assembled out of organic building blocks, they can be made bio-compatible [14]. Thus, they can be implanted and used in vivo without causing immune reactions. Organic layers are already used as coating material for in-situ electrodes to record neural activity [15]. More all-plastic, bio-compatible sensors are likely to be developed in the near future monitoring critical data like local blood pressure or blood sugar concentration.

With the organic origin of the novel materials, there is also a major drawback inherited. They easily degrade under environmental conditions due to humidity, oxygen and light [16, 17]. In fact, this is the major obstacle that has to be overcome before such products can be introduced into the consumer market. The principal limitation of organic materials is their confined lifetime. Requirements for many applications are in the range of several tens of thousands of hours. This is orders of magnitude beyond most numbers published to date. Encapsulation technologies as part of the packaging process play an important role to make such new systems ready for marketing [18, 19, 20].

The performance of the electronic devices built with organic materials nowadays is far from competing with the established silicon technology. But the idea is not replacement but expansion of the application of electronic devices into new low cost / low performance markets [21]. One example could be the so often mentioned RF-ID tag for supermarket products to simplify logistics and payment. But the field of possible applications is much wider once functional and durable devices can be mass produced. As important as the material itself are the technologies to fabricate functional devices as will be explained in the next section.

1.1.2 Fabrication technologies

Many of the new organic materials are soluble and can therefore be applied in liquid form. When the side groups of the building blocks of a polymeric material are modified, their solubility can be altered. This approach was successfully used for many materials such as poly(phenylenevinylene) (PPV)-derivatives [8]. Using this material, the first organic LED based on a polymer was made by spin-casting a solution processable precursor, as reported in [22]. The polymerization process was carried out after the thin film had been applied. If the electro-active molecules cannot be mixed

with a solvent to form a solution, dispersions may be available which still allow the application of liquid-based processing technologies.

Different methods are used to form thin films. Spin-coating is one of them and probably the most widely used due to its simplicity. Especially in laboratory applications this method has become a standard. The film thickness can be adjusted by setting the spin-speed and time. A drawback is the large amount of waste considering the quantity of material applied compared to the one effectively making up the thin film. Therefore, spin-coating is not often used for high volume fabrication. Another technique is dip-coating, where the sample is submerged into the solution and pulled out again. When the solution is applied to the substrate using a roller, the term roll coating is used. For large area processing, spraying is the most adequate method, since only the required material is applied.

One way to apply a patterned thin film is to use a screen printing process. Rubber stamping can be used as well as described in [23]. Other deposition and patterning techniques are based on the utilization of ink-jet printer technology enabling the solution-based organic materials to be directly printed on the substrate. Yet another way is to modify the surface characteristics of the carrier material to define hydrophobic and hydrophilic areas [24, 5]. A water based solution, for example, spreads on a transparency made of polyethylene only if the surface is modified first. This can be done by a masked plasma treatment process or, even simpler, with a laser printer since the surface of a black line has different properties than a blank area. For some organic electronic materials, standard lithography can be used, too [25]. Laser ablation is another way to pattern organic thin films with high accuracy, interesting especially for prototyping [26].

Insoluble organic materials such as Pentacene can be evaporated to apply thin films. Since the organic material might be degraded by the x-ray radiation in an e-beam evaporator, filament evaporators are commonly used. Since the process is performed under high vacuum, the films usually are of high quality.

All the technologies mentioned above are low temperature processes. This allows using substrates that would not withstand high temperatures such as most plastic materials. Flexible, all-plastic electronic devices can be built with the novel organic conductive and semiconductive materials and using the fabrication technologies explained above.

1.1.3 Sensor applications

The novel organic materials have also attracted attention from sensor developers. The prospect of cheap manufacturing prices makes them interesting candidates to build a new generation of sensors, completely made out of plastics.

One example where conjugated polymers can be applied as the active material are photodiodes. For the detection of visible light, organic devices which are both sensitive and fast have been already demonstrated [27, 28]. Infrared detectors can be built by using the effect that some oxidatively doped (p-type) materials show a very strong absorption in this particular region of the spectrum. Thus infrared radiation is detectable through a change in resistivity of the material [29]. The effect is due to a thermal effect as described in [30].

Another field of application is to utilize the electrochemical properties of the organic material to build ion sensing devices for chemical sensing. Conjugated polymers can be chemically doped to change their charge transport properties. The potential of a membrane made out of such a film immersed into an ionic solution depends on the ion concentration in the solution, which actually modifies the doping. Thus, ion sensors can be built [31, 32, 33]. The selectivity to certain species can be increased by modifying the chemical structure of the organic material. An example is a stable glucose sensor built this way [34].

For some applications not the intrinsic properties of the material are of interest but the fact that they can be used to build flexible electronic devices. One is to copy nature's successful design of a tactile sensitive skin to give robotic systems more information about the things they actually touch. Such a tactile sensor can be built on a flexible substrate by attaching stiff standard electronic circuitry and sensors at certain points [35]. Another way is to use flexible organic electronics for the first stage of amplification directly at the sensor element built into the skin. An example is given in [36] where a tactile sensor is detailed that is based on Pentacene OFETs to amplify the signal from a pressure sensitive rubber material.

To implement organic sensors, a piezoresistive, flexible layer that can easily be deposited would be very useful. Combined with organic electronic circuits for read-out and signal conditioning, the same fabrication technologies could be used to build integrated sensors. The approach of building

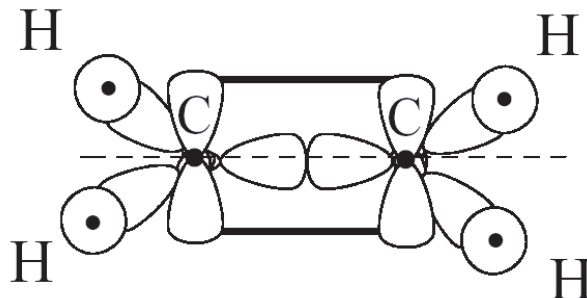


Figure 2: Sketch of an ethylene molecule with a double bond between the carbon atoms and single-bonds to the hydrogen atoms, adapted from [10]. The σ bond between the C-atoms is in the middle on the dashed line where two sp^2 -hybrid-orbitals overlap. The one π -bond is indicated by the two thick lines representing the overlap of two figure-8 shaped p-orbitals.

devices based on the same technology platform has already proven success in the field of CMOS integrated sensors [2, 3].

1.2 Charge transport in conductive and semiconductive polymers

Molecules are built out of individual atoms that are connected to each other. When pairs of electrons are shared between atoms, so called *covalent bonds* are formed. A single bond incorporates one shared pair of electrons. In case when two or three pairs of electrons are shared, a double bond or a triple bond, respectively, is formed. The orbitals of the four valence electrons in the outer shell of a carbon atom can be configured in different ways by overlapping, resulting in so called hybrid orbitals. When a carbon atom has four single bonds, the $2s$ -orbital and the three $2p$ -orbitals will form four equally shaped sp^3 -orbitals. All bonds between s -orbitals or hybrids of s - and p -orbitals are termed σ -bonds. In case the carbon forms a double bond, only the $2s$ - and two $2p$ -orbitals will hybridize to three sp^2 -orbitals. The unhybridized $2p$ -orbital will form the second bond of the double bond which is referred to as π -bond. Accordingly, the electrons forming this bond are called π -electrons. Such a π -bond is weaker in energy than a strong σ -bond. An ethylene (C_2H_4) molecule with a double bond between its two carbon atoms is sketched in Figure 2. One σ -bond in combination with two π -bonds is called a triple bond since three electron pairs are involved. The appearance of such a bond is shown in Figure 3 for an acetylene (C_2H_2) molecule. Only the $2s$ - and one $2p$ -orbital are hybridized to form two sp^1 -hybrid-orbitals, while the other two $2p$ -orbitals remain unchanged in their figure-8 shape [10].

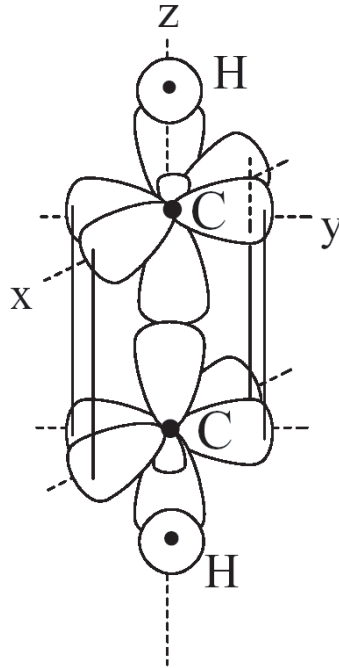


Figure 3: Sketch of an acetylene molecule with a triple bond between the carbon atoms and single-bonds to the hydrogen atoms, adapted from [10]. The σ bond between the C-atoms is in the middle where two sp^1 -hybrid-orbitals overlap. The two π -bonds are indicated by the four thick lines representing the overlap of the two figure-8 shaped p_x - and p_y -orbital-pairs.

Conjugated polymers consist of long carbon chains with alternating single and double bonds. In an infinite long chain, all bonds are equivalent and the π -electrons are delocalized along the whole chain. However, in shorter polymers the bonds at the ends have different properties because of the attached end-groups. A conjugated polymer itself might still be an insulator, as polyacetylene is for example, with a conductivity of $10^{-9} S/cm$. The resistance can be reduced by several orders of magnitude by chemical doping. Figure 4 shows the structure of polyacetylene during the doping process with iodine as reported in 1977 [4]. The halogenes (I_2) receive a weakly bound electron from the carbon chain and form a negatively charged ion (I_3^-). Electrons of the conjugated structure are attracted from the positive charge of the carbon atom that donated the electron. Thus, the charge becomes delocalized and can move along the chain. The polyacetylene molecule, positively charged after the p-type doping, is termed a radical cation, or polaron. The conductivity was raised to a value of $38 S/cm$ in the doped state. Nowadays, conductivities close to those of metals can be achieved [5]. Complete chemical doping to the highest concentrations yields reasonably high-quality materials. However, it is difficult to achieve intermediate doping levels since the results often

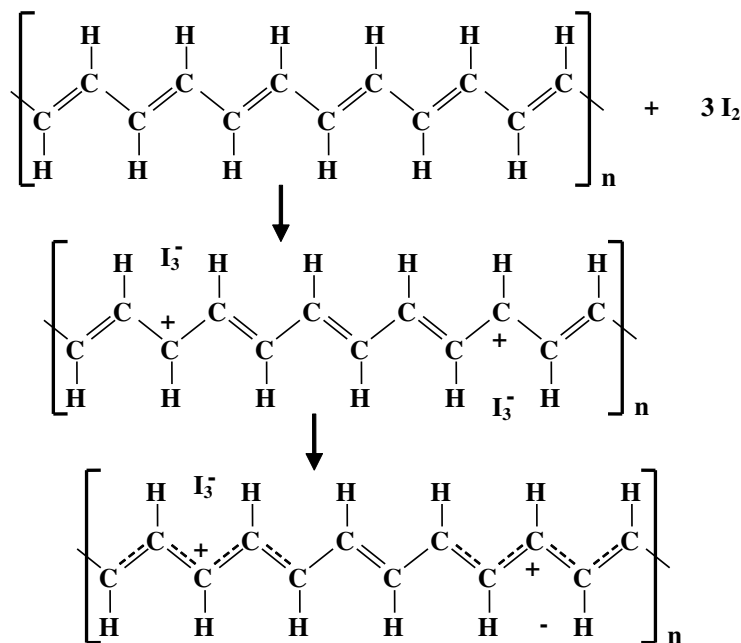


Figure 4: Doping process of polyacetylene with iodine. Top: the undoped structure. Middle: double bonds are opened and electrons have been transferred. Bottom: delocalization of the charges on the polymer chain. Adapted from [8, 6].

show inhomogeneities. Doping in an electrochemical active solution is also possible. The doping level can be adjusted and stabilized by controlling the potential between the counter electrode in the electrolyte and the conducting polymer [6]. This process is termed electrochemical doping. Photodoping can also be observed in some conducting and semiconducting organic materials [37].

In conjugated molecules, the p -orbitals of the π -electrons overlap. Thus, the arrangement of electrons is reconfigured concerning the energy levels. An example for six carbon atoms of a benzene ring is shown in Figure 5. The molecular energy levels can be separated into two categories: π and π^* or bonding and anti-bonding. They form a band-like structure. Since a pure band structure is found only in materials with completely delocalized charge carriers, such as in doped single-crystal silicon, the term is not accurate to describe intrinsic organic conductors. Only for an infinitely long chain, a band could be defined for the charge transport along the backbone. Nevertheless, the approximation of a band structure is useful to understand and describe the charge transport and other effects like photogeneration in organic materials. For these materials one rather speaks of molecular energy levels than of bands. The occupied π -levels are the equivalent of the valence band in crystalline semiconductors. The electrically active level is the highest one and it is called HOMO

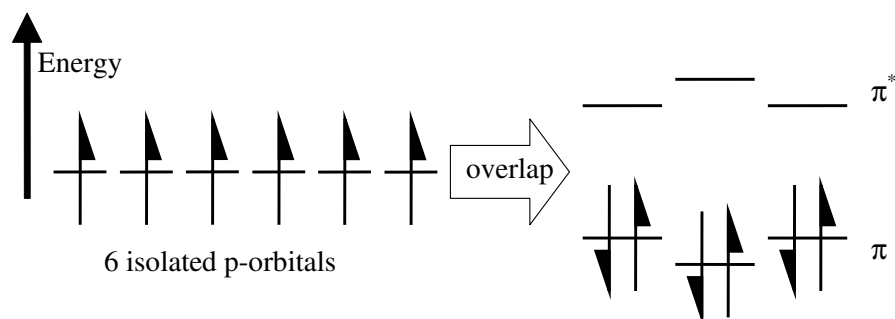


Figure 5: Mixing of degenerated p-orbitals leading to a band-like structure, adapted from [38].

(highest occupied molecular orbitals). The unoccupied π^* -levels are equivalent to the conduction band. Here, the electrically active level is the lowest of them, called LUMO (lowest unoccupied molecular orbitals). Between those two levels, a bandgap is formed. The structural characteristic of most electro-active polymers is their quasi infinite π -system extending over a large number of recurring monomer units. This feature results in materials with directional conductivity, strongest along the axis of the chain [38]. If the polymer chains are not ordered but randomly distributed, an amorphous material with anisotropic properties is formed.

So far, only the charge transport along conjugated polymers has been explained. A conductive path in an application with these materials can only be formed when the charge carriers are also transported from one chain to another. The process to describe this transfer is commonly called intermolecular hopping and is a thermally assisted tunneling effect [39]. The mechanism was originally proposed by Conwell [40] and Mott and co-workers [41]. A quantitative evaluation of the transition rates for this phonon-assisted tunneling is given by Miller and Abrahams [42]. The theory was originally developed to describe impurity conduction in silicon and germanium. But their work is also the foundation for several other models to describe the charge transport in disordered molecules [43, 44]. Disorder is not only introduced from the end-groups of conjugated polymer chains but also from defects in form of kinks, cross-links and impurities. Thus, the conduction critically depends on the hopping between conjugated parts of the polymer. The theories are also applicable to describe the charge transport in conducting and semiconducting organic materials such as conjugated polymers [45, 46, 47], oligomers and small molecules [48]. In the next section, the differences in their chemical structure will be explained in more detail.

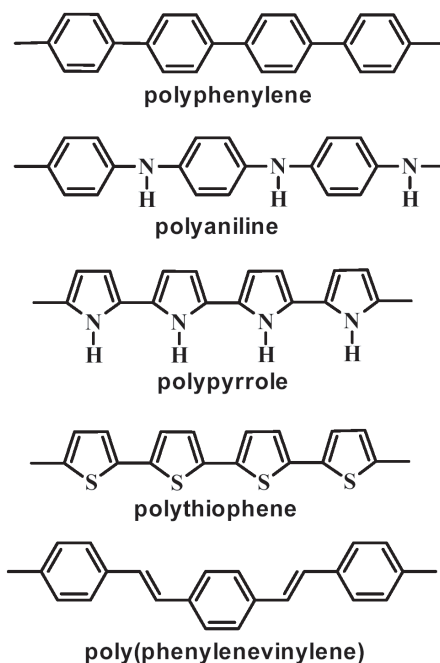


Figure 6: Chemical structure of selected conjugated polymers, from [8].

1.3 Materials

A broad variety of electro-active organic material is known and is ever-increasing. The substances can be classified in different groups based on their chemical structure.

1.3.1 Classification by molecular weight

Besides polyacetylene shown in Figure 4, there are many other polymers with delocalized π -electrons. Often they incorporate aromatic compounds, thiophenes and pyrroles. All of these groups have a ring like structure with alternating single and double bonds in common. Benzene rings with six carbon atoms are building blocks for aromatic compounds. In thiophenes, four carbon and one sulfur atom form a ring while the sulfur is replaced by a nitrogen atom in pyrroles. Some examples of conjugated polymers are shown in Figure 6. The building blocks for polymers are monomers which are connected to each other to form long chains during a polymerization process. When the chains of polymers are small, one rather speaks of oligomers than of polymers. Two oligomers are shown in Figure 7, structure a) and b). If a material is not made out of repeating units, it is usually classified as 'small molecule' although it might have a substantial molecular weight. Some

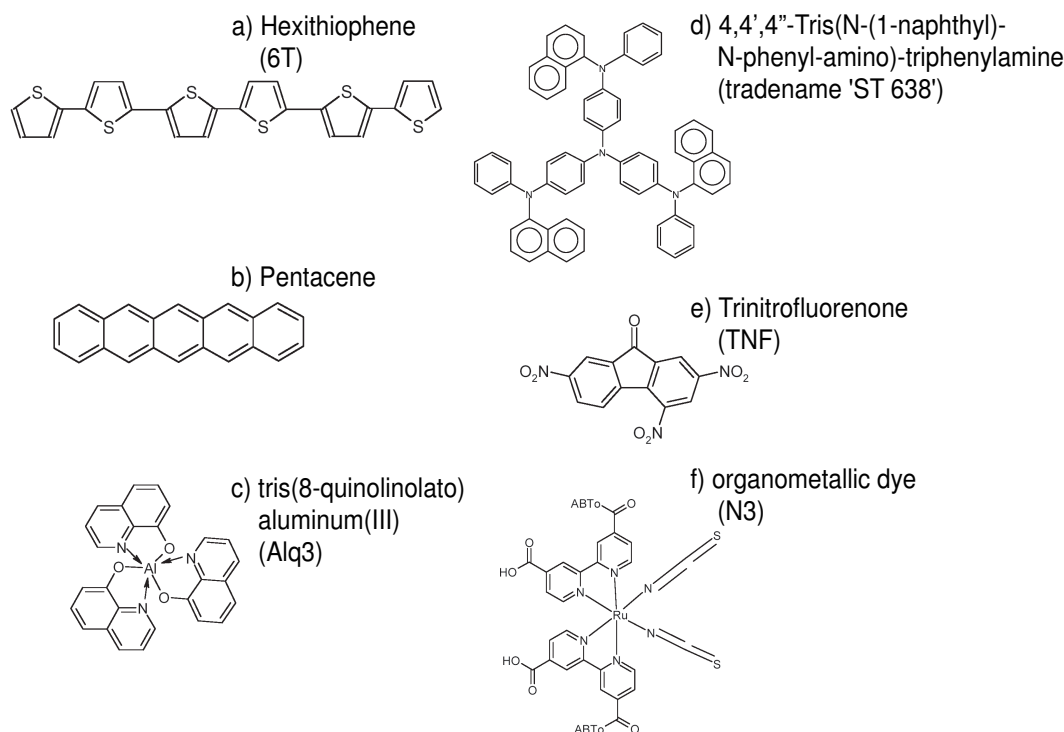


Figure 7: Chemical structure of selected electro-active oligomers and small molecules, adapted from [49].

small molecules are sketched in Figure 7, structures c) to f). Sometimes, the distinction is only made regarding the molecular weight. Polymers have a high molecular weight, oligomers and small molecules have a low one. *Hexithiophene* (6T) is one representative of the thiophene family of organic semiconductors [49]. In this case, six monomers are linked to form an oligomer. Polymers based on thiophenes are also widely used in organic electronic applications. They are well known for their high hole mobilities and are used in organic transistors as well as in organic metals. *Pentacene*, also a hole transporting material, is widely used in p-type organic transistors. For a high carrier mobility, a crystalline thin film structure is desired. Depending on the substrate and the deposition method used to apply the film, Pentacene has shown to form a highly ordered structure [50, 51] and thus high mobilities. Often, organic transistors are built on a silicon wafer with a smooth silicon oxide as gate insulator, but polymeric gate dielectrics can also be used [52]. *Alq3* is an organometallic complex with efficient green electroluminescence and remarkable stability. It was used as the emissive material in the first double layer organic light-emitting device [53]. *ST638* is a low molecular weight material but due to its architecture it has a very high glass transition temperature. Typically it does

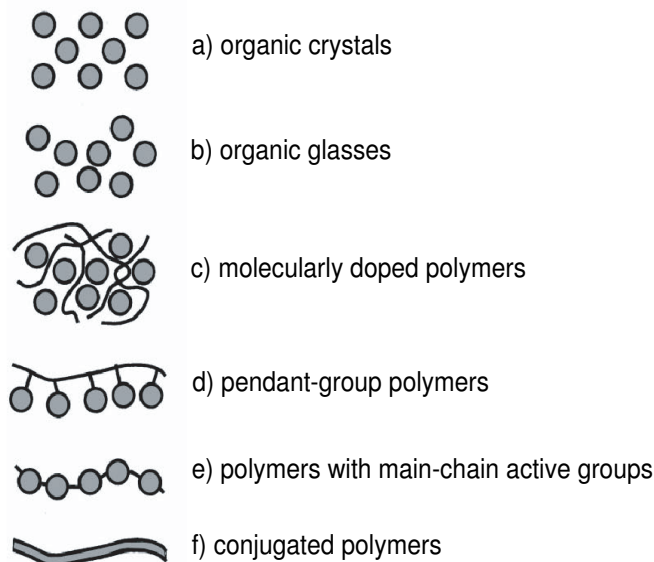


Figure 8: Schematic diagram depicting the classes of organic semiconducting materials, from [39]. The gray areas indicate the π -conjugated system.

not crystallize when spin-cast from solution but forms a glassy film [49]. It is successfully used as a thick hole transport layer for doped organic light emitting diodes [54]. *N3* is an organometallic dye with broad absorption spectra spanning the red and near infrared, which is often used for the harvesting of solar photons in dye-sensitized photovoltaic cells [49]. *TNF* is a common electron acceptor for the formation of charge transfer complexes with conjugated molecules [49].

1.3.2 Classification by structure

Another way to classify the materials is to distinguish them by physical order. Of great interest in the structure of the matter is where the electrical active π -conjugated parts are and how they are ordered. The typical schemes are shown in Figure 8. Pure low molecular weight materials like *Pentacene* or *Hexithiophene* form organic crystals or glasses when applied as thin films [55]. Small molecules such as dyes are often used as fillers in polymeric compounds for molecular doping [49]. An example for a pendant-group polymer is poly(vinylcarbazole) (PVK) [39]. In PVK, carbazole groups, which are conjugated small molecules, are attached to a polyvinyl backbone. Polymers with main chain active groups are often block copolymers such as MDNVB-TEO which is formed

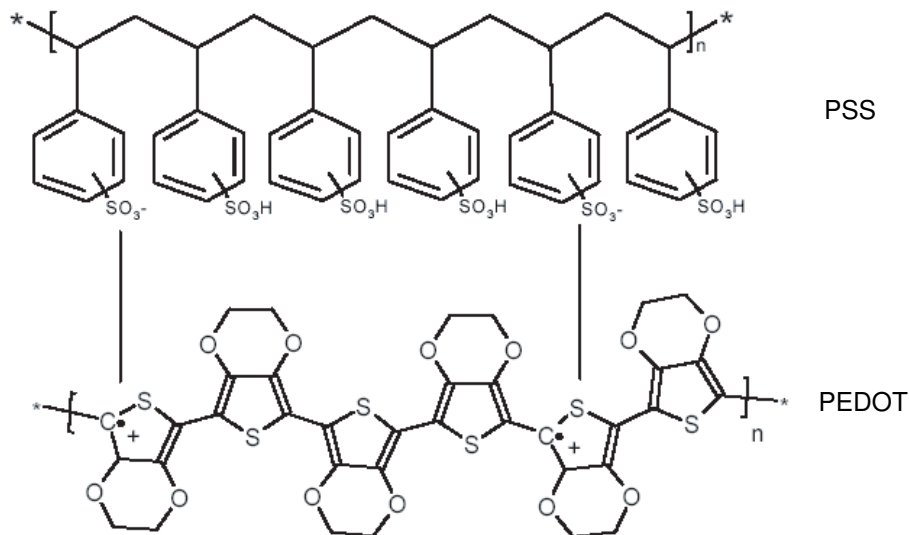


Figure 9: Structure of PEDOT doped with PSS, adapted from [49].

from 2,5-dimethoxy-1,4-di(a-(2-naphthalene vinylene)benzene) and tri(ethylene oxide) [56]. Typical conjugated polymers with delocalized electrons along the whole main chain are shown in Figure 6.

1.3.3 PEDOT:PSS

PEDOT is the abbreviation of poly(3,4-ethylenedioxythiophene) and is one of many derivatives of the thiophenes. It is a conjugated polymer built from ethylenedioxythiophene (EDOT) monomers. PSS stands for poly(4-styrenesulfonate) and is also a polymer. Each styrene ring of the monomer has one acidic SO_3H group. The chemical structures are shown in Figure 9. PEDOT is one of the most successful materials among the synthetic metals. It possesses several advantageous properties such as a low oxidation potential and moderate bandgap with very good stability in the doped state. Due to its chemical structure, it also forms a high regiochemically defined material [57]. Other alkylendioxythiophene derivatives have been studied as well and show mostly similar behavior but also vary in some respects. The reader is referred to [57] and to [58] for more detailed information about the derivatives.

PSS is the most often used dopant for PEDOT. The doping process of the conjugated polymer is done by acid- rather than redox-doping. Thus, the PEDOT does not act as an electron donor but accepts a proton from the sulfonate group of the PSS dopant. A $\text{C}=\text{C}$ π -bond of the EDOT opens

up and the C bonds to an H^+ donated by the acid. As a result, there is a net positive charge on the PEDOT chain that will strongly attract the negative charge left on the acid. Since this happens at many points along the polymer, PEDOT and PSS become closely intertwined. An unpaired π -electron remains on the PEDOT chain that is highly mobile along the conjugated backbone and leads to a high conductivity [57]. Other dopants reported in literature include Tosylate [59] and inorganic materials such as Phosphomolybdate [60].

PEDOT:PSS was originally developed as antistatic coating for photographic films. In the automated process of developing, the plastic film material can accumulate static charges and discharge sparks may expose the film. A conductive coating, even with a rather low conductivity, can prevent the build-up of high voltages. For this application PEDOT:PSS is successfully used and the fabrication volume of coated photographic film per year exceeds 10^8 m^2 . Additionally, it is used for packaging microelectronics components [49]. Other applications include electrode material in solid-state capacitors, substrates for electroless metal deposition in printed circuit boards and electrode material in organic electroluminescent lamps [57]. Due to the high work function of PEDOT, it is also a good material for making anodes in light emitting devices [61, 62]. Finally, it is a useful electrode material for organic photovoltaic cells, where somewhat higher sheet resistance is not a problem because of the generally low current densities [49].

Aqueous dispersions of PEDOT:PSS are commercially available under the trade name Baytron[®] from Bayer. With this material, thin, highly transparent and conductive surface coatings can be prepared by spin-casting or dip-coating onto almost any hydrophilic surface. Bayer offers a variety of dispersions for different applications. Depending on solid content, doping concentration, particle size and additives, films with different conductivities result thereof. The bandgap for Baytron[®] P is given with approximately 1.6 eV and the work function is approximately 5.2 eV . The dispersion is acidic with a pH value between 1.5 and 2.5 at room temperature because of the PSS content. There is a variety of coating formulas available, specified for the diversified applications.

Another way to produce PEDOT films or fibers is to use electropolymerization. The polymerization is not chemically activated but potentiostatically in solutions containing the monomer EDOT. In situ measurements of PEDOT films grown this way are presented in literature [63]. Properties of polymer nanofibers are given in [64].

Recently, flexible and transparent PEDOT:PSS-coated polyester sheets with sheet resistances of the order of $1k\Omega/\square$ have become available under the trade name Agfa OrgaconTM. These sheets can be patterned by an etching procedure which is very similar to conventional photoresist patterning, although the chemistry involved is rather different. This is a potential substrate material onto which future organic electronics and displays can be prepared [49].

1.4 Piezoresistivity

Piezoresistivity is one of the most often used transducer effects, in particular for electromechanical sensors made out of silicon. Typical applications are pressure sensors, accelerometers, resonant micro structures used e.g. for chemical sensing [3] and for force sensors for atomic force microscopy (AFM) [65]. The reason for the common use of the piezoresistive effect is its simplicity.

1.4.1 General description of the piezoresistive effect

The name 'piezo' comes from the Greek word 'piezin' which means squeezing or pressing tightly. Combined with resistivity it describes the dependence of electrical resistivity ρ on a mechanical strain ϵ or stress σ . The formula is usually given in terms of stress σ applied to the resistor. For isotropic materials in the linear elastic region, the stress-strain relationship is given by Hooke's law

$$\sigma_x = E \cdot \epsilon_x \quad (1)$$

with the Young's modulus E . The strain ϵ is defined as the relative change in length ($\epsilon = \Delta l/l$).

The linear piezoresistive effect in one direction in an isotropic material is defined by

$$\frac{\Delta\rho_x}{\rho_x} = \pi_x \cdot \sigma_x \quad (2)$$

The piezoresistive coefficient π has units of Pa^{-1} . To describe the piezoresistive effect for isotropic materials in all three dimensions including normal and shear stress components, the coefficient π must be defined as a tensor and thus equation 2 becomes

$$\frac{\Delta\rho_i}{\rho_0} = \sum_j \pi_{ij} \cdot \sigma_j \quad (3)$$

The indexes describe the geometrical orientation of the effect. The stress component, j defines the three normal stresses and the three shear stresses. In the contractive notation, six components are

Table 1: Denotation of the contractive notation used for the piezoresistive coefficient π

contractive notation	denotation
1	x-x
2	y-y
3	z-z
4	y-z and z-y
5	x-z and z-x
6	x-y and y-x

used as summarized in Table 1. To describe the directionality of the resistivity, the same relationship between voltage and current can be applied as between stress and strain. Therefore, the index i has six components as well.

In the contractive notation, the general piezoresistive coefficient π becomes a second rank tensor with 6×6 elements.

$$\pi_{ij} = \begin{bmatrix} \pi_{11} & \pi_{12} & \pi_{13} & \pi_{14} & \pi_{15} & \pi_{16} \\ \pi_{12} & \pi_{22} & \pi_{23} & \pi_{24} & \pi_{25} & \pi_{26} \\ \pi_{13} & \pi_{23} & \pi_{33} & \pi_{34} & \pi_{35} & \pi_{36} \\ \pi_{14} & \pi_{24} & \pi_{34} & \pi_{44} & \pi_{45} & \pi_{46} \\ \pi_{15} & \pi_{25} & \pi_{35} & \pi_{45} & \pi_{55} & \pi_{56} \\ \pi_{16} & \pi_{26} & \pi_{36} & \pi_{46} & \pi_{56} & \pi_{66} \end{bmatrix} \quad (4)$$

For anisotropic materials, the number of independent components can often be reduced due to symmetry effects. For example, in single-crystal silicon there are only 12 non-zero coefficients instead of 36. Due to the cubic crystal symmetry, only three of them are independent: π_{11} , π_{12} and π_{44} . For isotropic material, the number of independent components can be reduced to only two.

For most applications, only two arrangements of load and resistance change are of interest, resulting in the longitudinal and the transverse piezoresistive effect. The first one describes the change of the resistance if the force is applied in the same geometrical direction as the E-field and thus the current is flowing, while the second one describes the change to a load applied perpendicular to the E-field and the current direction. An illustration is given in Figure 10. Under a), the resistor is stretched by the force F in the same direction as the current is flowing when a voltage is applied between the electrodes. Thus, the longitudinal piezoresistive effect has to be taken into account. In

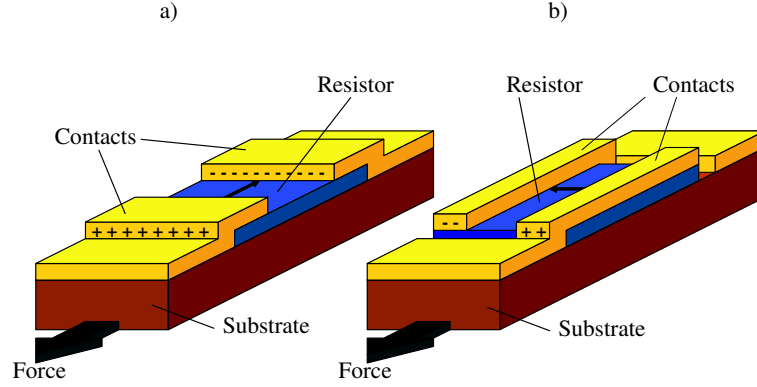


Figure 10: Piezoresistor under a) longitudinal and b) transverse stress. The small black arrow on the resistor points in the direction of the current.

b), the current is flowing perpendicular to the direction of the applied force F constituting a transverse piezoresistive effect. Both structures can be easily build and used to characterize the different piezoresistive effects. The effective values for the longitudinal piezoresistive coefficient (π_L) and the transverse piezoresistive coefficient (π_T) can be calculated from the piezoresistive coefficient tensor π_{ij} . For anisotropic materials such as single-crystal silicon, (π_L) and (π_T) depend on the orientation of the resistor with respect to the crystal axis and the values can be computed using coordinate transformation techniques. For an unknown, isotropic material, the values of π_L and π_T can be identified directly by using appropriate test structures, e.g. the resistors shown in Figure 10. A description of the linear piezoresistive effect can then be given by superposition of the longitudinal and the transverse piezoresistive effect:

$$\frac{\Delta\rho}{\rho} = \pi_t \cdot \sigma_t + \pi_l \cdot \sigma_l \quad (5)$$

with the stress components σ_l in longitudinal and σ_t in transverse direction.

1.4.2 Geometrical effect

A change of resistance due to an applied load to a resistor is also caused by geometrical effects. Any material with a finite elastic modulus will be deformed when stressed, following equation 1 and including that the strain ϵ is defined as $\Delta l/l$. Since the resistance depends on the geometry of a resistor as defined in equation 6, it will alter if the dimensions are changed.

$$R = \rho \cdot \frac{l}{A} \quad (6)$$

Here, A is the cross sectional area the current is flowing through and is defined as width w times thickness t . The length of the resistor is given by l and ρ is the specific resistivity of the material and usually given in $\Omega \cdot \text{cm}$.

To determine the effect of a load to a resistor, one also has to consider the transverse contraction of the material. The effect is described by the dimensionless Poisson ratio ν

$$\epsilon_y = -\nu \cdot \epsilon_x \quad (7)$$

linking the strain ϵ in x- and y-direction. Assuming that a resistor with length l is experiencing a strain ϵ in the length direction, its width w and thickness t will change according to

$$l^* = l(1 + \epsilon) \quad (8)$$

$$w^* = w(1 - \nu \cdot \epsilon) \quad (9)$$

$$t^* = t(1 - \nu \cdot \epsilon) \quad (10)$$

The variables marked with an asterisk describe the dimension after the resistor is stretched. Inserting these definitions into equation 6, one can calculate the resistance of the stretched material. The resulting equation can be simplified assuming that the strain is much smaller than one ($\epsilon \ll 1$). The change of resistance $\Delta R/R$ due to the geometrical effect in longitudinal direction is then described by

$$\left[\frac{\Delta R}{R} \right]_l = \epsilon(1 + 2\nu) \quad (11)$$

The same approach can be used to determine the transverse effect. By modifying the dimension accordingly, the resulting description for the transverse geometrical effect is thus given by

$$\left[\frac{\Delta R}{R} \right]_t = -\epsilon \quad (12)$$

The previous derivation is valid for bulk material assuming it is isotropic and for small changes in dimensions only. All the resistors investigated for this work have been made by applying a thin conducting film on a substrate material. Since the stiffness of the thin film is very small compared to the much thicker support, its contribution to the total stiffness can be neglected. The thin film will be stretched by the same amount as the substrate is. This assumption is valid for the directions of the width w and the length l of the resistor as long as the bonding is good. Thus, the material properties

of the substrate determine the geometrical effect. This is not valid for the change in thickness t since the film is not constrained by the support in that dimension. Unfortunately, data about the mechanical properties of the PEDOT:PSS thin films used in this investigation were not available. Since the Poisson ratio ν does not vary much, especially for the same class of material, the value 0.34 valid also for the polyimide substrate was used for the thickness change.

1.4.3 Effective change of resistance due to load

In the previous subsection, only the geometrical aspect was considered but not the change in resistivity caused by stretching or compressing a resistor as given in equation 2. Combining the piezoresistive and the geometrical effect, a description of the effective change in resistance is obtained. By applying the superposition principle the following equations are found for the longitudinal and the transverse resistance change respectively.

$$\left[\frac{\Delta R}{R} \right]_{l_{effective}} = (1 + 2\nu + \pi_l \cdot E) \epsilon \quad (13)$$

$$\left[\frac{\Delta R}{R} \right]_{t_{effective}} = (-1 + \pi_t \cdot E) \epsilon \quad (14)$$

The product $\pi \cdot E$ is also referred to as the piezo component α_p or the K-factor and is dimensionless. Often, the effective change of resistance is described by the Gage Factor GF which is defined in equation 15. Its value is typically used to calculate the strain out of measurements from metal strain gages.

$$GF = \frac{\Delta R/R}{\Delta l/l} = \frac{\Delta R/R}{\epsilon} \quad (15)$$

1.4.4 State of the art for piezoresistive sensors

Common applications for metal strain gages can be found in industry to measure the strain on mechanical components. They are used for static applications as well as for measuring vibrations. The resistors are usually long and thin because of the high conductivity of metals. This is also favorable as they are often mounted onto the sample and an increase in stiffness due to the sensor is not desired. The standard method of measuring the change of resistance is to set them up in a Wheatstone bridge configuration. Metal strain gages are also widely used for sensor applications, for example in pressure sensors [66]. Some designs are shown in Figure 11. They are also used

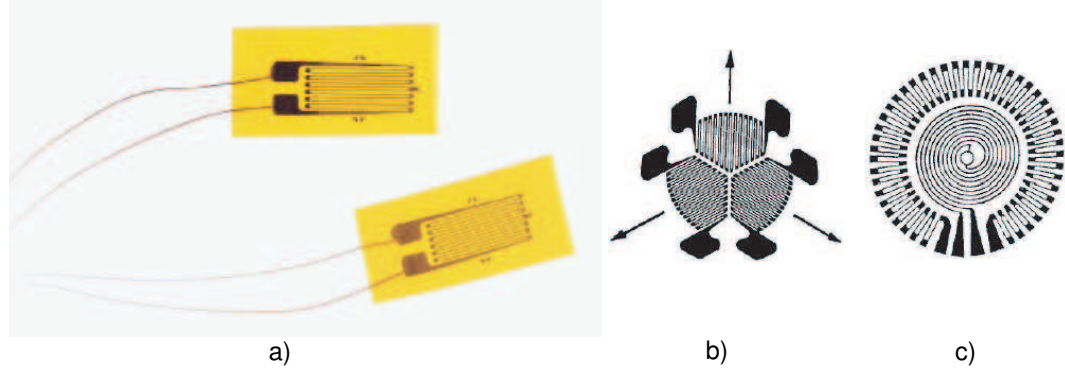


Figure 11: Examples for metal strain gages: a) Meander shaped structure for industrial applications. b) Strain gage for multi axial strain measurements. c) Design of a metal strain gage on the membrane of a pressure sensor. Adapted from [66].

Table 2: Gage factor and piezoresistive component α_p for selected metals.

Metal	Gage Factor GF	piezoresistive component α_p
Aluminum	2.5	0.84
Gold	2.1	0.22
Copper	2.2	0.47
Platinum	4.0	2.24

in MEMS-based applications because they can easily be fabricated out of thin films deposited on the mechanical structure. For example, flow sensors and tactile sensors which are built with nickel-chrome piezoresistors on a liquid crystal polymer substrate have been reported [14]. In metals, the piezoresistivity is mainly caused by a change in the mobility of the electrons. This is due to the effect that the amplitude of the thermal vibration is affected by a volume change of the material. The effect is small and in the same order of magnitude as the geometrical effect. The piezoresistive component α_p is always positive, meaning that the resistance increases when the sample is stretched. For most metals and alloys, the gage factor is decreasing with increasing temperature [66]. Data to describe the piezoresistivity of some metals are summarized in Table 2.

Sensors made out of single-crystal silicon utilizing the high intrinsic piezoresistive effect are commonly used. The piezoresistive coefficients depend on the direction along the crystal axis, doping type, doping level and on temperature. The maximum values at room temperature and at low doping levels of $10^{16}/cm^3$ are summarized in Table 3. The magnitude of the piezoresistive

Table 3: Maximal piezoresistive coefficients for doped single-crystal silicon at room temperature and for low doping levels. For p-doped resistors the maximal effect is found at an angle of 45° , for n-type resistors at 0° with respect to the $\langle 100 \rangle$ direction on a (001) wafer. Data from [68].

Material	longitudinal, π_l	transverse, π_t	Gage Factor, longitudinal
p-doped	$71.8 \cdot 10^{-11} Pa^{-1}$	$-66.3 \cdot 10^{-11} Pa^{-1}$	126
n-doped	$-102.2 \cdot 10^{-11} Pa^{-1}$	$-53.4 \cdot 10^{-11} Pa^{-1}$	-128

effect decreases with increasing temperature. Therefore, measures have to be taken to compensate for the temperature dependence. For higher doping levels, the piezoresistive coefficients but also their temperature dependence decrease. Sometimes the sensitivity of a device is traded for higher temperature stability for applications operating at a wide temperature span. In silicon metal-oxide-semiconductor field-effect transistors (MOSFETs), a strong piezoresistive effect is found as well and a characterization can be found in [67].

Polycrystalline silicon exhibits a piezoresistive effect, too. Since the silicon grains are oriented randomly, the piezoresistive coefficients of single-crystalline silicon have to be averaged over all crystal directions, resulting in a reduced effect. In addition, the influence from the grain boundaries has to be taken into account. The piezoresistive effect in polysilicon is isotropic and therefore independent of direction and can be fully described with the longitudinal and transverse coefficients π_l and π_t . The values depend not only on the doping level but also on deposition and annealing conditions of the film. For example, the piezoresistive components for the longitudinal α_p and the transverse α_p are 30 and 14, respectively, for a polycrystalline silicon film deposited by low pressure chemical vapor deposition to a thickness of $0.5 \mu m$ and annealed at 950° . The investigated film is p-doped by boron ion implantation with 60 kV to a level of $10^{18}/cm^3$ [68].

A tactile sensor relying on the combination of highly sensitive silicon piezoresistive elements and polymers as the dominant material concerning the mechanical properties of the device is described in [69]. To build this shear force sensitive artificial skin, thin silicon cantilevers are embedded perpendicular to the surface in a thick polymer layer. Under shear stress, they deform and the resulting change in resistance can be read out. Applications are in the field of robotics, where such sensors would allow optimizing the required force to manipulate objects.

An approach to utilize polymeric materials as piezoresistive sensing layer is to use compounds

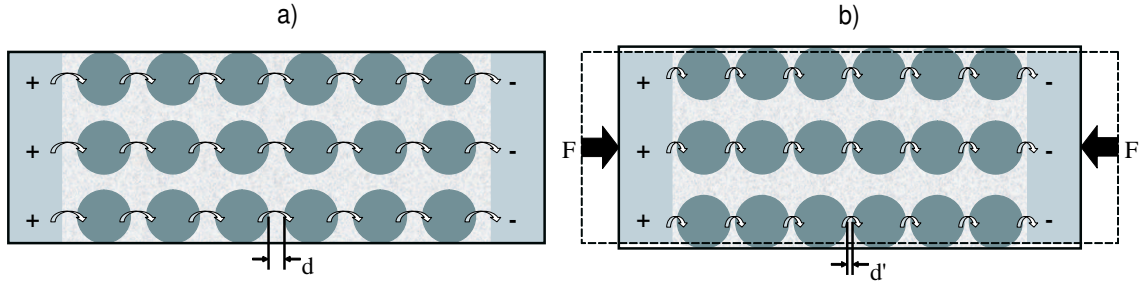


Figure 12: Piezoresistor made from a polymer with conductive filler (circles). a) unstrained, b) with applied load. The distance d between the filler particles is reduced to d' .

of polymers with low conductivity and highly conductive fillers, e.g. metal or graphite powders. A schematic of the structure of such a material is shown in Figure 12. Since the filler is much stiffer than the polymeric matrix, the load leads to a deformation of the polymer but hardly of the filler. Thus, the size of the filler particles does not change but the distances between them. The composite can be considered as a network of metal-polymer-metal junctions connected in series and in parallel. Depending on the charge transfer mechanism between the conductive particles, the change in distance between them can have a great impact on the overall conductivity. For the case of a space charge limited conduction (SCLC) mechanism, a theoretical derivation and comparison to measurement results is presented in literature [70]. The reported material combinations are polyvinylidene fluoride and polyphenylene sulfide as polymers and copper or carbon black as fillers added to a volume fraction between 2% and 20%. The characterization of a benzophenone tetracarboxylic dianhydride-oxydianiline/metaphenylene diamine polyimide matrix film used in a compound with submicron-sized graphite particles is given in [71]. Mechanical and electrical properties have been investigated for different compositions ranging from 15% to 25% by weight for the graphite loading. A maximum gage factor of 16.8 at 18% graphite loading was found. The magnitude of the piezoresistive effect strongly depends on the volume fraction of filler in the polymer compound. Therefore, to achieve material with a high gage factor, the graphite content must be exactly controlled. The film was not applied as a sensing layer on an existing mechanical structure but formed a membrane itself. Highly structured nano-size conductive carbon black particles used as filler in a polyisoprene matrix and their piezoresistive effect are investigated in [72]. A change of electrical resistance by

more than four orders of magnitude is observed at 40% relative stretch. The nanocomposite exhibited a very weak semiconductor-like temperature dependence of resistance and the piezoresistive effects was found to be practically stable in the region of 20°C to 70°C but is nonlinear over strain.

A pressure sensor based on a poly(methylmethacrylate) (PMMA) membrane and using multi-walled carbon nanotubes (MWNT) as sensing elements is described in [73]. The MWNT bundles were formed across previously patterned gold electrodes using a dielectrophoretic technique. Experimental results led to an average estimated gage factor of approximately 235 for the piezoresistive carbon nanotube sensing element, this is about twice the value of the maximum effect found in single-crystal silicon. A deeper insight into the charge transfer mechanism of carbon nanotube films is given in [74] and in [75]. Doped and undoped films were investigated and gage factors of 125 and 65 respectively were found. The measurements were performed in air and at room temperature. The origin of the piezoresistive effect is supposed to be a band gap change for the doped films and intertube contact resistance variations for the undoped tubes similar to the effect found in polymer composites. A general overview of carbon nanotube based sensors is also given in [33].

An approach to obtain a piezoresistive material on a purely organic basis has also been reported [76]. A blend of piezoelectric poly(vinylidene fluoride) (PVDF) with polyaniline was investigated for resistance changes due to compressive loads to the samples. The current-voltage relationships were nonlinear for all doping levels, indicating a space charge limited conduction mechanism. A piezoresistive effect was found which was also depending on poling time and strength done to the samples prior to measurements. A gage factor or a piezoresistive coefficient was not explicitly reported.

Fabrics made out of Lycra fibers which are coated with the conductive polymer polypyrrole (PPy) were investigated by De Rossi et al. [77]. Gage factors for strains up to 1.2 % are given with -13.25 in longitudinal and -12.5 in transverse direction. Compared to measurements taken on thick films of PPy with resulting values of 0.45 to 0.9 for the gage factor, the effect is largely emphasized by the deposition on textile fibers. Also, a negative temperature coefficient was reported for this material.

CHAPTER II

SAMPLE PREPARATION

To investigate the piezoresistive behavior of PEDOT:PSS, thin film resistors out of this material were fabricated for tensile testing in different variations. A flexible plastic substrate was used for the strain experiments. Some samples were also prepared on glass as a reference. Two types of PEDOT:PSS aqueous solution were applied by spin-coating on the substrate. To form metal contacts, gold or silver was deposited on top of the resistive layer. The pattern of the electrodes was defined by shadow masking. The final device structure is shown in Figure 13.

2.1 Substrate material

As flexible substrate, Kapton[®] polyimide film was chosen because of its good mechanical and chemical stability. Furthermore, its properties are well known and published. The material is used in many fields, in particular in electronic applications for high density circuit boards or as flexible substrate [78] and as insulator in motors and other parts [79]. Especially the high temperature stability makes it a good choice for many tasks. Kapton[®] type HN is used successfully in applications at temperatures as low as -269°C and as high as 400°C . The standard Kapton[®] type HN with a thickness of $125\text{ }\mu\text{m}$ was used in this work for all experiments involving stretching of the substrate. To determine the elastic modulus of the material, stress-strain curves were measured using a Dage 4000 shear tester. The data shown in Figure 14 was taken at room temperature. For small strains ($\epsilon < 0.4\%$), the stress-strain relationship is approximately linear. The Young's modulus was calculated out of the measurements and the extracted value for $E = 3.1\text{ GPa}$ is close to the one given from the supplier of the Kapton[®] foil, DuPont [79] of 2.96 GPa at 22°C .

Glass was used as a reference for some experiments. Although these samples were not stretched to investigate a change in resistance due to a load, they did prove useful for the general electrical characterization of the applied thin film resistors. Standard microscope slides were taken as substrate in this case.

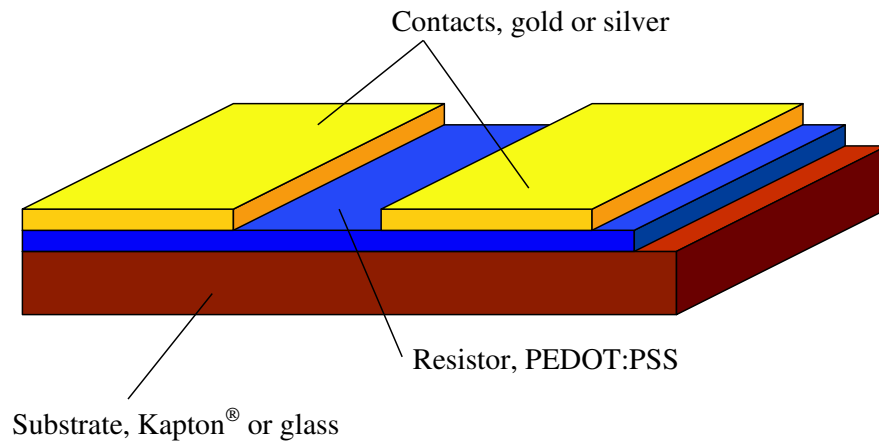


Figure 13: Device structure for PEDOT:PSS resistors.

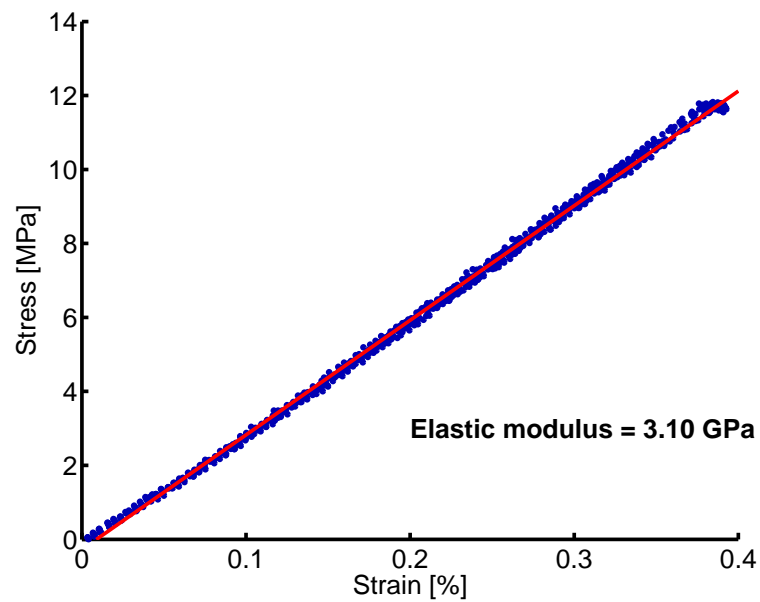


Figure 14: Stress-strain relationship of Kapton® 500 HN polyimide foil. The dots represent data from 7 successive measurements of the same sample at room temperature. The solid line is a linear curve fit and the slope is equal to the elastic modulus ($E = 3.1 \text{ GPa}$). [Measurements courtesy of Dr. W. H. Song, ETH Zürich, Switzerland]

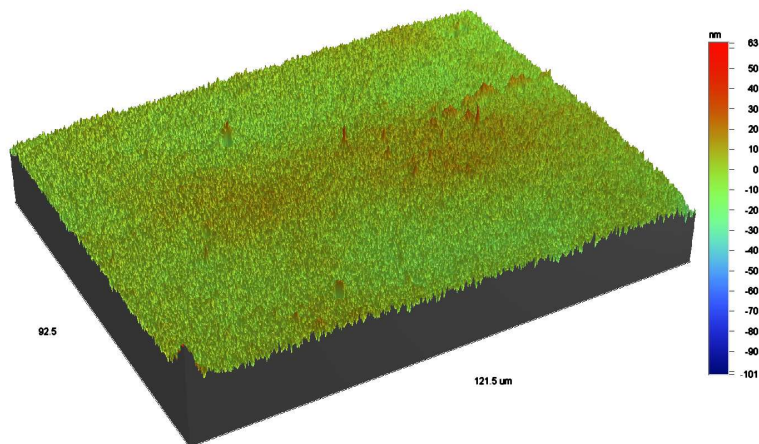


Figure 15: Surface roughness of a microscope glass slide (50x magnification). The full color range corresponds to $0.164 \mu\text{m}$

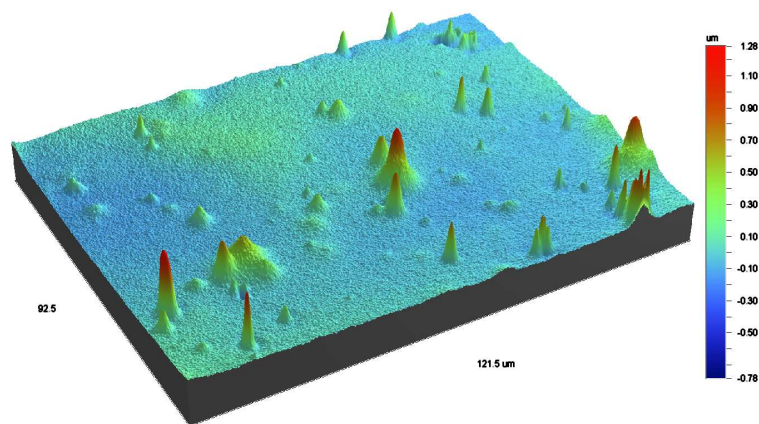


Figure 16: Surface roughness of Kapton® 500 HN front side (50x magnification). The full color range corresponds to $2.060 \mu\text{m}$

To spin-cast the electrical active layer on the substrate, the surface structure is of great importance. Baytron® PEDOT:PSS is an aqueous solution and does not cover a hydrophobic surface very well. Therefore, the polyimide base material has to be treated accordingly to modify its surface to become hydrophilic. Also, the surface roughness may have an impact on the morphology of the spin-cast film. Kapton® HN was found to have a much higher surface roughness than glass as shown in Figures 15 and 16. The surface-scans shown were obtained from a non-contact optical white light interferometer.

2.2 *Cleaning procedure*

The substrates, both glass and Kapton[®] films were cleaned in order to avoid contamination before the active layer was applied. The cleaning procedure comprises four steps:

- Liquinox
- DI-water
- Acetone
- Methanol

All steps were carried out in an ultrasonic bath with each step lasting twenty minutes. Liquinox is a phosphate-free laboratory detergent used to remove organic compounds from the sample surface. Residues of the detergent were washed off with DI-water. The samples were then dried with nitrogen. To remove organic substances such as grease, the samples were put in Acetone and afterwards in Methanol. Once again they were dried using nitrogen before the samples were stored in a closed box to protect them from dust. For handling reasons, the thin Kapton[®] sheets were mounted on glass slides using double sided tape. The size of a typical sample was 20 mm x 20 mm.

2.3 *Preparation of PEDOT:PSS resistors*

Since Kapton[®] is hydrophobic, all samples were treated for two minutes in an oxygen plasma prior to the film deposition. This resulted in good hydrophilic surfaces on which the aqueous solution of PEDOT:PSS was spin-cast. A good description of the surface chemistry of polyimides and suitable surface treatments is given in [80]. Samples with high conductivity were prepared by using Baytron[®] P, low conductivity samples were made with Baytron[®] P VP AI 4083. To achieve different film thicknesses, the parameters of the spinner were varied from 4000 rpm down to 3000 rpm, 2000 rpm and 1000 rpm. Below 1000 rpm, the films are not uniform anymore. To achieve thicker films, several layers were cast on top of each other successively. The spinning time was always set to sixty seconds. Since the water of the thin film evaporates quickly, the films dry easily within minutes. For the multi-layered samples, the time between two subsequent deposition steps was typically five minutes. Finally, to remove the water solvent completely, the samples were heated

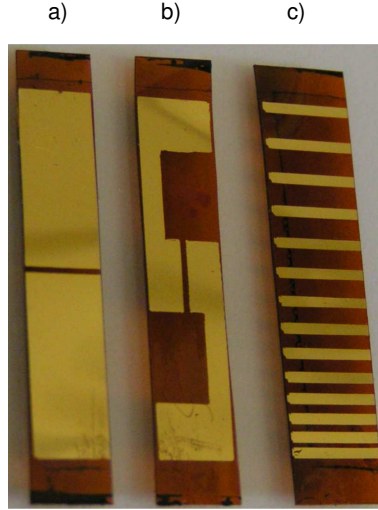


Figure 17: Photograph of some fabricated samples: a) Resistor to measure longitudinal piezoresistive effect. b) Resistor to measure transverse piezoresistive effect. c) Test structure with different channel length.

to approximately 90°C for two hours in a vacuum oven. To avoid the absorption of humidity, the samples were then stored in a desiccator under a constant dry nitrogen flow.

Top side contacts for the resistors were made with a metalization process. Gold or silver was applied in a filament evaporator under high vacuum. The geometry was defined by shadow masking the active area. The thickness of the metal layer was approximately 1000 \AA for both materials used.

A photograph of some fabricated samples with different device structures is shown in Figure 17. A resistor to measure the longitudinal piezoresistive effect is shown in a). The current will flow in the same direction as the stress will be applied. A resistor to characterize the transverse piezoresistive effect is displayed in b). The resistor is aligned perpendicular to the length of the sample and thus to the strain when stretched. In c), a test structure of 13 resistors with different length can be seen. The shadowmasks for the metalization of these devices was fabricated by laser-cutting of a polyimide film.

2.4 Physical device characterization

The geometrical dimensions of the structures under test have been measured using an optical microscope with an attached CCD-camera. Each pixel in the magnified image corresponds to a certain

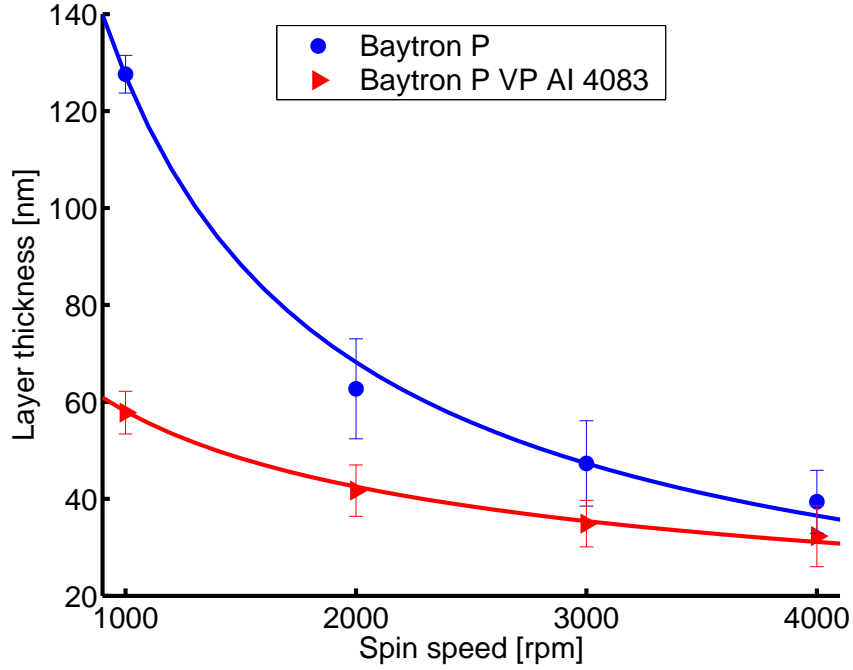


Figure 18: Layer thickness of PEDOT:PSS spin-coated on glass. The dots represent the mean value of the measurements taken, the error bars show the standard deviation and the solid line a curve fit according to equation 16.

distance on the sample and thus dimensions in the xy-plane can be accurately measured. Nevertheless, it was found difficult to determine the exact borders of the metalized contacts. Since they have been fabricated using shadow masks in a non-contact mode, there is a transition region between the fully shadowed area and the metal layer. In this approximately $10 \mu m$ wide area, the metal contact looks diffuse in an optical system since thin enough metal films become almost transparent.

The metal film thicknesses were monitored with a resonant quartz micro-balance during deposition and were verified by measurements with a stylus profilometer. Therefore, profiles of clearly defined steps which have been created by covering part of the samples were recorded.

For the resistors, the final layer thicknesses of Baytron® P and Baytron® P VP AI 4083 on glass were determined by scratching away part of the spin-cast film and measuring the step with a stylus profilometer. The measured film thickness as a function of the spin-speed is shown in Figure 18. The dependence of the thickness t of a spin-coated film on the physical conditions is given in a general form in equation 16.

$$t = \frac{s \cdot k}{(rpm)^q} \quad (16)$$

Table 4: Parameters for curve fit of thickness as a function of spin speed for PEDOT:PSS films (see Figure 18. Values for s are given in the product information brochures from Bayer [81], values for k and q are found by fitting the measured data with equation 16.

	Baytron[®]	
parameter	P	P VP AI 4083
s	1.30%	1.80%
k	3823	40
q	0.9	0.45

While the spin-speed (rpm) can usually be adjusted on the spin-coater, the solid contents s and the constant k are fixed for a given solution. Often, a square root dependence ($q = \frac{1}{2}$) on the spin-speed is found, but for the investigated films a better fit was obtained for values other than one half. The determined coefficients for the curve fit shown in Figure 18 are given in Table 4. The dependence of layer thickness on spin-speed is consistent with data provided in [82] for Baytron[®] P. Both dispersions, Baytron[®] P and Baytron[®] P VP AI 4083, were used as delivered without any further additives. The thickness of the spin-cast PEDOT:PSS on Kapton[®] could not be determined, because the surface is relatively rough as shown in Figure 16. Since the plastic material is much softer than glass, the surface might be scratched as well when trying to remove part of the spin-cast film. If a section of the film is wiped off directly after the spin-cast procedure, the material tends to smooth out the step and can not be measured accurately.

CHAPTER III

CHARACTERIZATION

Samples fabricated from Baytron[®] P and Baytron[®] P VP AI 4083 were characterized by measuring their resistance under different conditions. To investigate the piezoresistive behavior, the samples were mechanically stretched and the resulting change in resistance was recorded. The impact of environmental influences was examined by either taking measurements under inert gas atmosphere or exposing the samples to ambient conditions. For the characterization of the temperature dependence of material properties, samples were externally heated and the resistance was measured simultaneously. The self-heating effect of the resistors was also utilized to investigate the temperature influence.

3.1 Film resistance without mechanical stress

To determine the difference between the PEDOT:PSS layers spin-cast on glass and on Kapton[®], measurements were taken on test structures with different resistor lengths under ambient conditions. Contacts to the test structure were made by using a probe station. The results for samples coated with Baytron[®] P at a spin-speed of 1000 *rpm* are shown in Figure 19. On glass, a film thickness of 128 *nm* was measured for this sample. Both curves can be reasonably well interpolated with a linear fit. Thus, the resistance must be linear dependent on the resistor length l . This is the case for ohmic behavior. Other charge transport mechanisms such as space charge limited conduction can be excluded, since there, the current density J_{SCLC} has a different dependence on l :

$$J_{SCLC} = \frac{9}{8} \epsilon_0 \epsilon_r \mu \frac{V^2}{l^3} \quad (17)$$

The measured resistances converge towards zero for decreasing resistor length l , indicating that contact resistances can be neglected.

All data points lie close to an ideal linear fit through the origin, clarified with the dashed lines shown in Figure 19. Therefore, the conclusion that the film thicknesses on both samples are the same

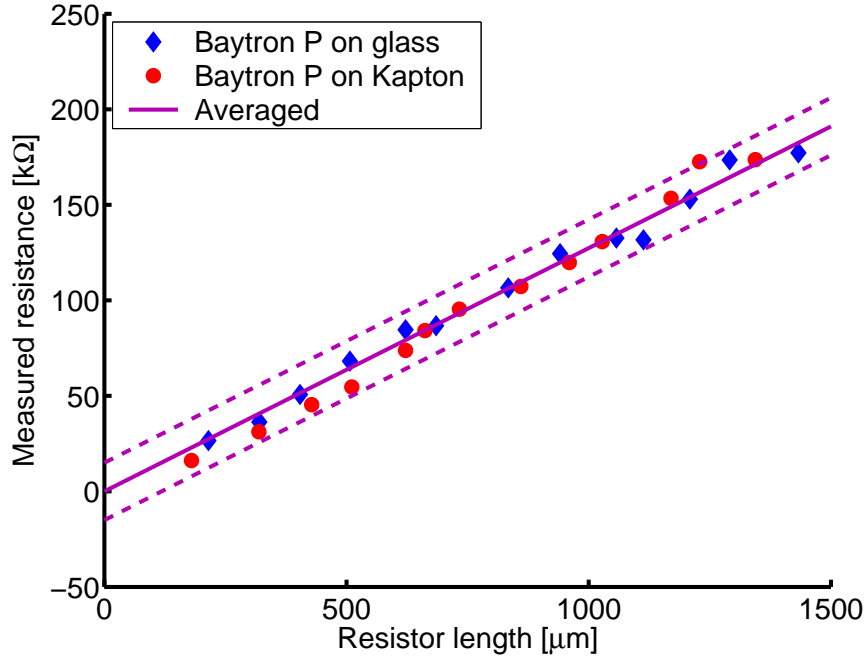


Figure 19: Measured resistance of Baytron® P on glass and on Kapton® as a function of the resistor length. The dashed lines represent the maximum offset of the measured values from the linear curve fit. The width w of the resistor is 5 mm and the film thickness t is 128 nm.

is reasonable. Since the thickness of the PEDOT:PSS layer on Kapton® could not be determined, the reference values obtained from the glass samples can be used for any calculation involving the film thickness. The average resistivity extracted from these measurements for the particular sample is $8.28 \Omega \text{ cm}$. This is considerably larger than the value stated in the datasheet for Baytron® P of approximately $1 \Omega \text{ cm}$ [81]. The given value is for bulk material, while in the present work thin films are used. Measurements on other samples showed that the resistivity for Baytron® P varies from $2 \Omega \text{ cm}$ to $10 \Omega \text{ cm}$. Seifert et al. investigated the electrical characteristics of spin-cast PEDOT:PSS layers with thicknesses from 190 nm to 380 nm [25]. Their work concludes that both, resistivity and contact resistance increase with decreasing film thickness. The resistivity value determined in this work does match well with their evaluation.

For the low conductivity grade PEDOT:PSS, Baytron® P VP AI 4083, the measured resistivity lay between $1000 \Omega \text{ cm}$ and $7000 \Omega \text{ cm}$. The value given from the supplier is $1000 \Omega \text{ cm}$ [81].

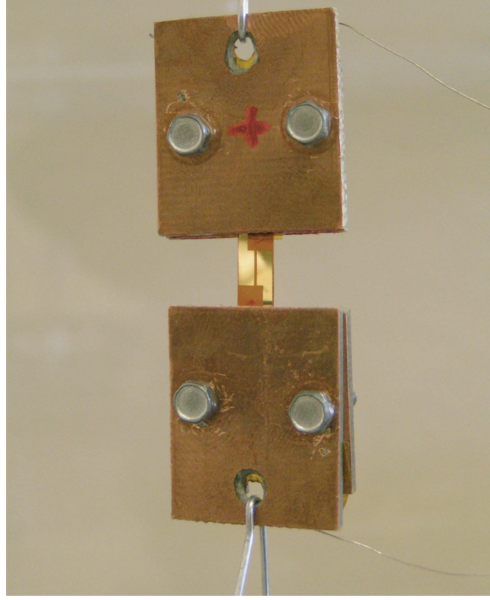


Figure 20: Photograph of measurement fixture with a sample to measure the transverse piezoresistive effect.

3.2 *Film resistance under mechanical load*

To investigate the piezoresistive behavior of the samples, measurements were taken with changing mechanical load applied to the devices. To this end, the samples were mounted in a mechanical clamp system. In order to actually stretch them, a weight was attached and because of the gravity a defined force was pulling on the device. For a typical set up, a sample with a width between 2 mm and 20 mm was mounted into the fixture, so that the distance from the clamp to the active region of the resistor was approximately 2 mm on both sides as shown in Figure 20. The exact position in the fixture was not measured. Using the basic mechanical equations for strain, stress and force (equations 18 to 20), it is possible to calculate the strain from the dimensions, the known Young's modulus E for the substrate and the acceleration of gravity g (9.81 m/s^2)

$$\epsilon = \frac{\sigma}{E} \quad (18)$$

$$\sigma = \frac{F}{A} \quad (19)$$

$$F = m \cdot g \quad (20)$$

yielding

$$\epsilon = \frac{m \cdot g}{E \cdot A} \quad (21)$$

with the applied mass m . The cross-sectional area A is defined by the product of the width of the sample w and the thickness t of the Kapton® substrate. The mechanical impact of the spin-cast PEDOT:PSS film can be neglected as it is very thin compared to the substrate and it is not expected to have a much larger elastic modulus. Typical values for the strain ϵ at maximum load are around 2 %.

The measurements were performed in a low oxygen / low humidity environment. Therefore, a desiccator, usually used as a storage device, was modified. A fixture was mounted inside to suspend the sample. A weight was attached using a monofilament string fed through a hole leading to the separated, lower chamber. The weight could be lifted to release the force working on the sample by pulling two other strings leading through a hole to the outside. Thus, the load of the sample could be changed easily without disturbing the inert gas atmosphere. The desiccator was flushed with dry nitrogen from the top inlet with 20 SCFH (standard cubic feet per hour). To ensure that most of the oxygen and humidity was driven out of the chamber, the nitrogen was turned on at least four hours before the measurements were started. A thermometer / hygrometer from Sensirion [83] was placed inside the chamber to monitor the room temperature and the relative humidity (RH). Typical values were 22°C and an RH value of less than 2 %. For measurements in ambient environment, the N_2 flow was stopped and the doors of the desiccator were opened allowing air in the chamber.

In order to measure the resistance of the sample inside the desiccator, a feed-through for electrical contacts was made. The sample was connected via thin, flexible wires to avoid any additional force to it. For the electrical measurements, a Keithley 6487 Picoammeter [84] with built-in voltage source was used. The internal power supply provides voltages up to 500 V and allows measurements even for large resistances above 100 M Ω with high accuracy.

For experiments at elevated ambient temperature, a heating stage was placed inside the desiccator. The controller and wiring was led outside and the chamber was sealed during the measurements to keep the nitrogen atmosphere. Samples inside the heater could be measured only in an unstressed state.

Most measurements were done with a load of 1 kg that was lifted while measuring the resistance to determine the response of the sample. A typical curve for one such cycle is shown in Figure 21. At time equal zero, the measurement voltage was applied. For the first 28 seconds, the load is applied

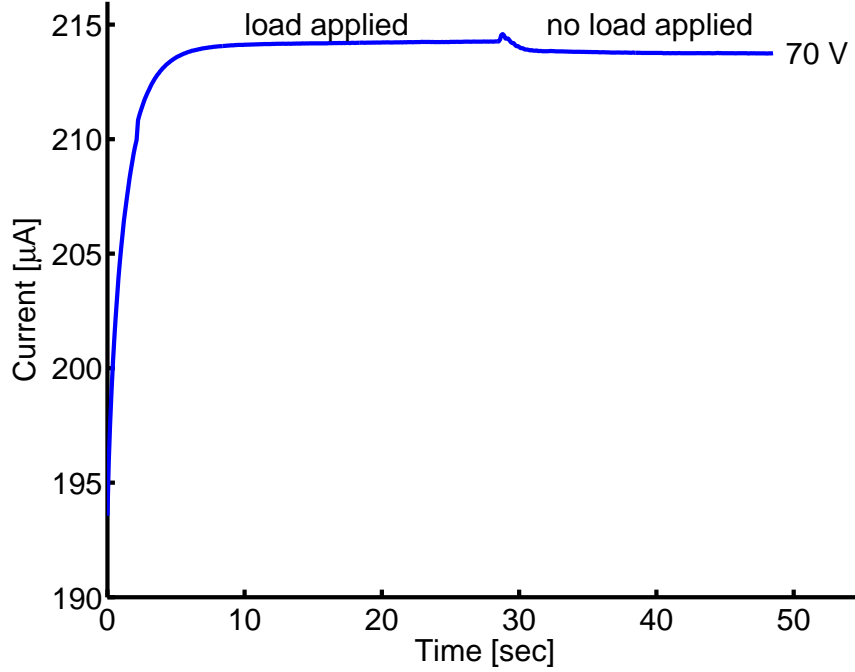


Figure 21: Typical measurement curve for changing load on a PEDOT:PSS thin film resistor, here for a sample with a 63 nm thick layer of Baytron[®] P and a sample size of $w = 2.04 \text{ mm}$, $l = 0.92 \text{ mm}$ on a 125 μm thick Kapton[®] substrate. The load of 1 kg was applied from the beginning and lifted after 28 seconds. The voltage source is connected at $t = 0 \text{ s}$.

to the sample. After 28 seconds, the weight was pulled up, putting the sample in the stress-free state. The change in current with constant measurement voltage can be seen.

Some measurements were performed with varying loads from 100 gram to 1 kg in 100 gram increments. As an example, Figure 22 shows the resulting resistance change as a function of the applied load. As expected, the change of resistance increases linearly with increasing load to the sample.

3.3 *Environmental influences*

As mentioned in the introduction, the stability of the organic materials used in electronic devices is a serious issue. Basically, all conjugated molecules degrade under the influence of O_2 by oxidizing the molecule. Since electrons in an excited state are highly reactive, they can easily bond to any available oxygen. Accordingly, the degradation under the same environmental condition is increased by temperature as well as by higher electrical activity. This is because more excited electrons will be available in both cases and the probability of oxidation is further increased. The effect is illustrated

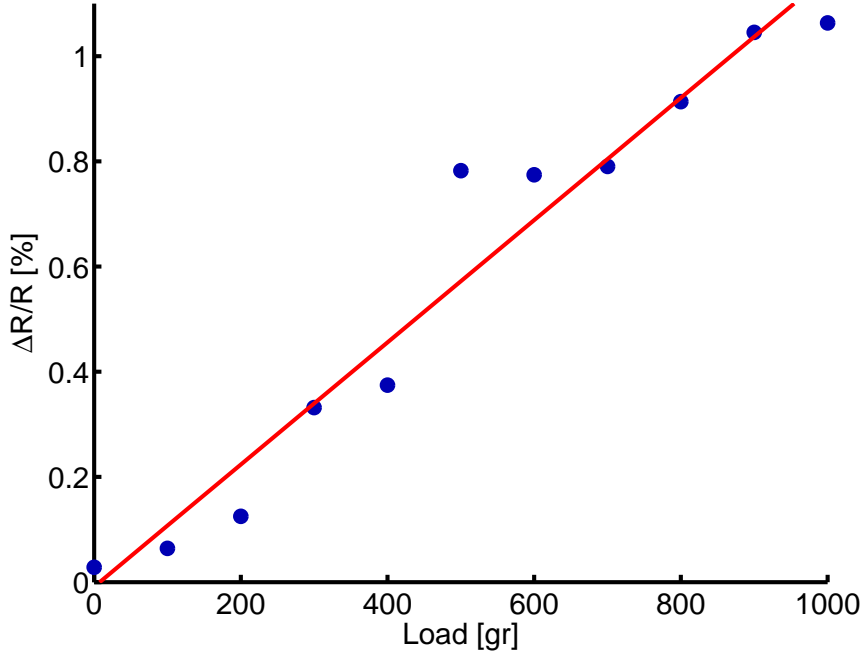


Figure 22: Change in resistance as a function of the applied load, measured for a sample with a 42 nm thick layer of Baytron® P VP AI 4083 at 500 V.

in Figure 23(a). For this particular measurement, the nitrogen supply was turned off after one hour of measurements and the desiccator was opened to let ambient air flow into the chamber. An immediate increase in resistance by about 44 % can be seen. Over the next hours, the resistance was continuing to increase slowly. In Figure 23(b), the sample was measured again after further degradation in air (42 hours). To find out if the process is reversible, the desiccator was closed and the nitrogen switched on again. Interestingly, the resistance does not decrease to close up to its original value but increases by several orders of magnitude to settle down after about one hour. When the air is let in again, the resistance drops even further than the value of the degraded state. It increases again once the nitrogen is turned on. Thus it seems that after the first degradation process of the sample when exposed to air, another conduction mechanism is dominant which reversibly depends on either oxygen or water (humidity) concentration of the surrounding atmosphere. Since the process is reversible, it might be suitable for sensor applications. A design of a humidity sensor built with a PEDOT:PSS resistor and a Nafion proton conducting membrane has already been published [85].

In the present work, it was discovered that the noise of the measured current is much smaller when the measurement is performed under nitrogen atmosphere than when done in air. Two relative

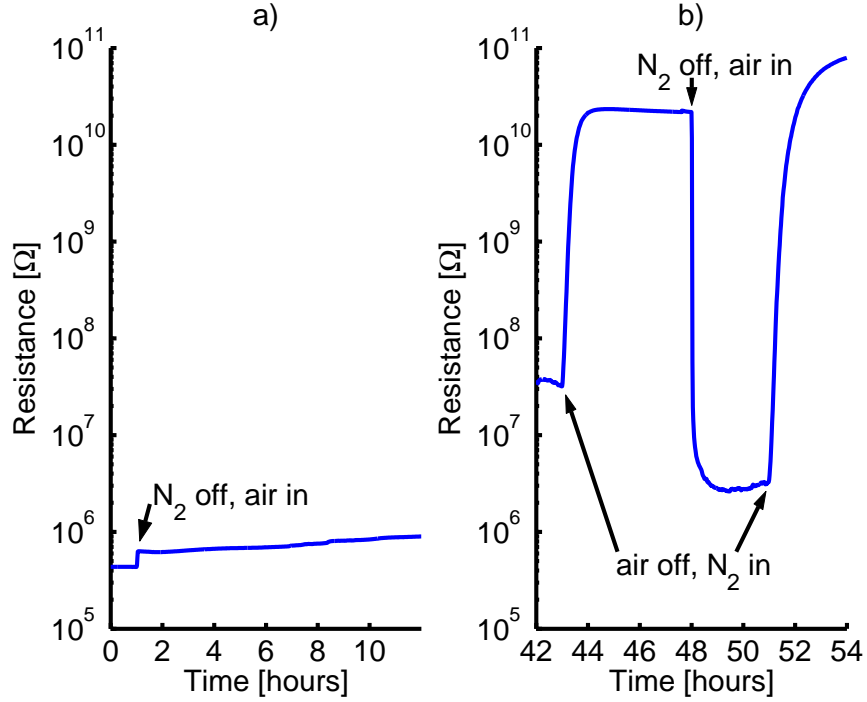


Figure 23: Effect of ambient conditions on resistance of PEDOT:PSS. Measurement curves for a sample with a 63 nm thick layer of Baytron® P. a) Exposure of the sample to air for the first time. b) Response of the same sample to further changes of the ambient conditions.

current curves of the same sample are shown in Figure 24. Note that the y-axes have the same scale. The resistance of the PEDOT:PSS resistor is about 20 MΩ in air and 2 GΩ under nitrogen. Although the current is higher for the sample in air and a lower noise floor would be expected for a constant signal to noise ratio for the same setup, the jitter is much higher for measurements taken under ambient conditions. It is most likely that oxidative doping and trapping of charge carriers play a role in the origin of this effect. The sample is already in the low conductivity state as described in the previous paragraph and shown in Figure 23(b). Since the low resistance is degraded quickly in presence of air and humidity when measured, the evaluation of the piezoresistivity was done under inert gas atmosphere. The sample measured in the desiccator flushed with nitrogen showed much better stability and lower noise (see Figure 24).

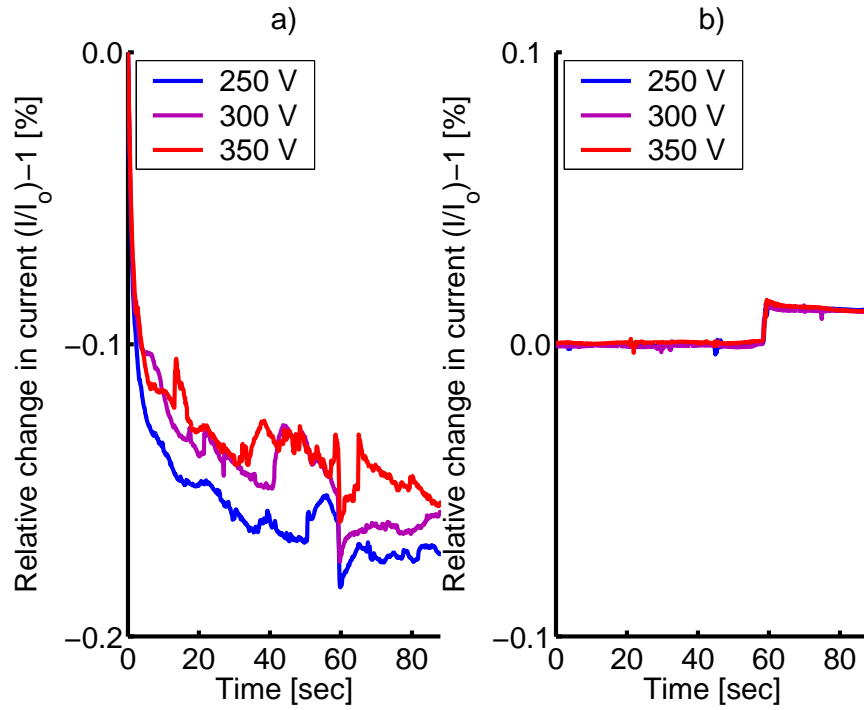


Figure 24: Effect of ambient conditions on noise in PEDOT:PSS resistors. Measurement curves for a sample with a 42 nm thick layer of Baytron® P VP AI. For both measurements a load change from 1 kg to 0 kg was done after 60 seconds. a) shows the measured values recorded in air while b) was measured under N_2 .

3.4 Joule heating

The effect of Joule heating was found in all samples prepared with Baytron[®] P and to a smaller extend for those prepared with Baytron[®] P VP AI 4083. The resistive power if operated at a constant voltage is less in the latter ones due to the higher resistivity of the thin film. The maximum voltage is limited to 500 V by the measurement equipment. A Joule heating effect of PEDOT:PSS resistors is also reported in literature [30] and was utilized to build infrared detectors [29]. The Kapton[®] polyimide used in the present work as substrate material has a low coefficient of thermal conduction ($\sigma_{th} \approx 0.12 \frac{W}{m \cdot K}$, [79]). In contrast, the metal electrodes have a much higher thermal conductivity, but their effect is limited by the small layer thickness. Thus, the energy transport by thermal conduction away from the heat generating resistive area is poor and as a result the sample heats up. Assuming a cantilever with length l , cross-sectional area A and thermal conductivity σ_{th} , the temperature elevation ΔT of the tip due to a power P dissipated at the tip is given by

$$\Delta T = \frac{P \cdot l}{\sigma_{th} \cdot A} \quad (22)$$

To evaluate the temperature rise of the investigated PEDOT:PSS resistors, their structure can be approximated as two cantilever beams connected at their tip. Since the copper sheets on the surface of the fixture are good heat conductors, the temperature at the clamping will be assumedly fixed at room temperature level. Equation 22 predicts then a linear dependence between temperature elevation and power. To identify the Joule heating effect, a sample was placed under an infrared camera system to measure the temperature contact free. Different voltages were applied to the resistor while measuring its temperature. A qualitative image of the temperature distribution is shown in Figure 25. The orange-pink-colored region in the middle of the picture is the resistor area, the yellow-green-blue areas on top and at the bottom of it are the metalized contacts. The thin, bright bars in-between are caused by the round edges of the metal contacts that lead to wrong readings of the IR-camera and do not represent the real temperature there. As can be seen, the general distribution meets the expectations of a sample with uniform heat generation and thermal conduction toward the clamping on top and bottom with the hottest spot in the center. The small divergence of the position of the hot spot is blamed on the non-uniformity in layer thicknesses of the PEDOT:PSS film due to the spin-cast process resulting in variations of the resistance. The nature of

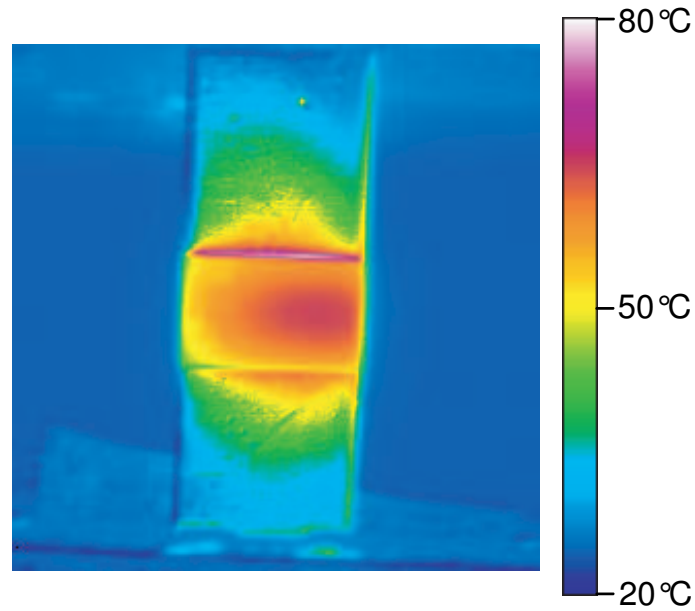


Figure 25: IR-image of temperature distribution in a self-heated PEDOT:PSS resistor sample with a 63 nm thick layer of Baytron® P on a 125 μm thick Kapton® substrate. The applied measurement voltage was 90 V and power consumption was 24 mW. Measurement was performed in ambient atmosphere.

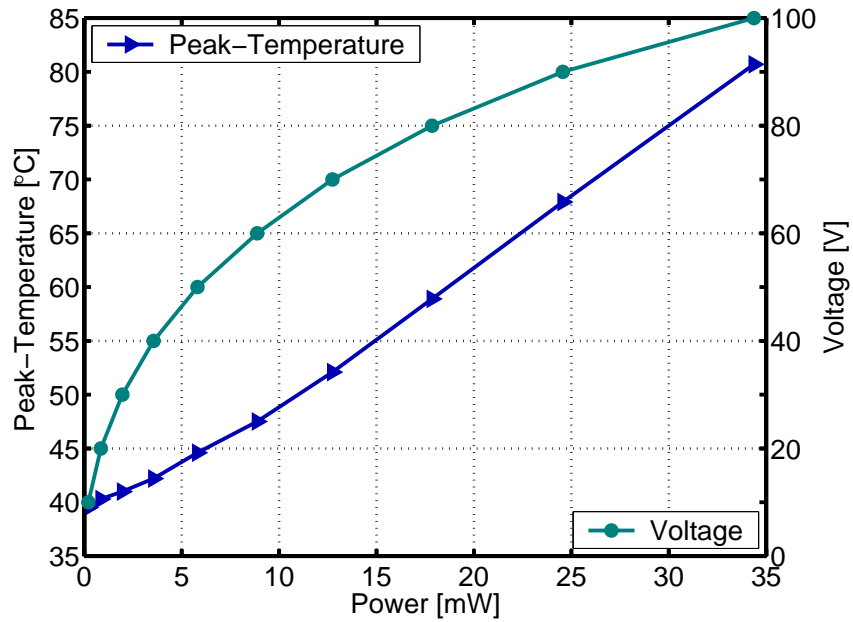


Figure 26: Peak temperature of a Joule heated sample with a 63 nm thick layer of Baytron® P on a 125 μm thick Kapton® substrate measured with an IR-camera under ambient conditions.

the contact-less temperature measurement technique requires a calibration step which was only done roughly. Therefore, the graph in Figure 25 gives a good overview of the behavior but no absolute temperature data. Also, the measurement could not be performed under an inert gas atmosphere but was done at ambient conditions in air. The peak-temperature of the sample as a function of electrical power consumption is shown in Figure 26. The temperature increases almost linear with power as predicted from equation 22. In contrast to the recorded peak-temperature measured at one point on the sample, the power is dissipated within the overall volume of the resistor. The deviation between the plotted peak-temperature as a function of power and an expected straight line, especially for small powers, might thus be explained because the heating effect is not uniform and the temperature can diffuse in less heated parts of the sample.

The effect of Joule heating is also responsible for the time dependence of the measured currents when different voltages are applied to a sample. As an example, Figure 27 shows the current through a PEDOT:PSS resistor as a function of time for different measurement voltages. The voltage is applied at $t = 0$, resulting in an increasing current during the first 20 seconds of the measurement interval. Figure 28 shows the relative current change with respect to the current at $t = 0$ for the data of Figure 27 to make the change in current clearly visible for all voltages. The current is rising caused by the Joule heating and thus increasing the resistor temperature and reducing its resistance. The relative current $I(t)$ follows close to an exponential function of the form

$$I(t) = I_{max} \left(1 - e^{-(t/\tau)} \right) \quad (23)$$

The time constant τ for the particular sample investigated in Figure 28 was found to be 3.5 seconds. The value depends on the geometry of the sample and the clamping conditions.

Joule heating of a resistor made from high conductivity PEDOT:PSS, such as Baytron® P, on a plastic substrate can be implemented for applications where heating to temperatures up to about 120°C is required. The film can easily be applied by spin-casting or dip-coating and the support material with its low thermal conductivity provides the necessary thermal insulation. In the present work, self-heating is used to characterize the temperature dependence of the observed piezoresistive effect. But Joule heating might also become a problem among organic electronic devices built on plastic substrates if the power consumption reaches critical values.

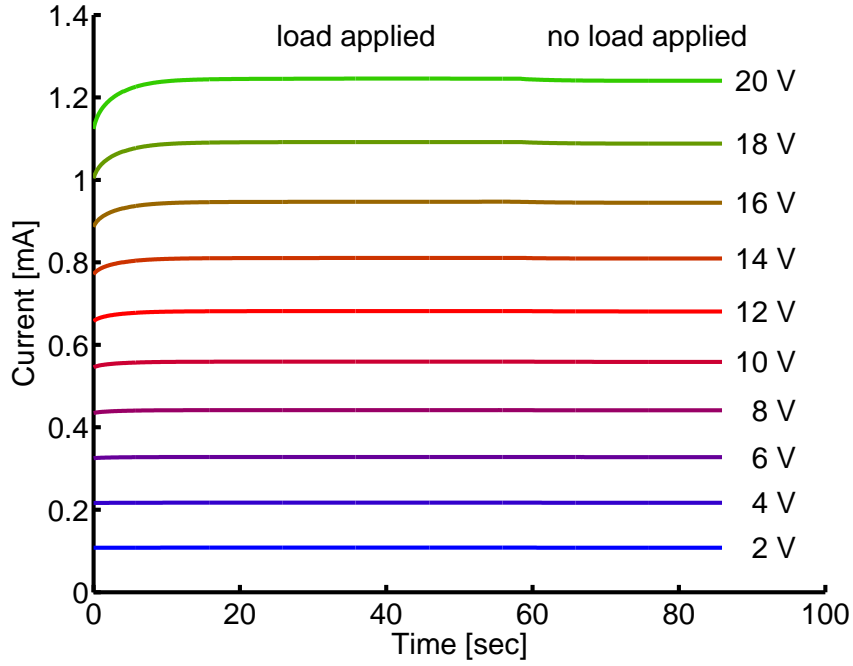


Figure 27: Current through a sample with 128 nm of Baytron® P on a 125 μm thick Kapton® substrate for different measurement voltages. The voltage is applied at $t=0$ sec. The rise of the current during the first few seconds indicates the Joule heating effect. For the first 58 seconds, the load is applied and removed afterwards.

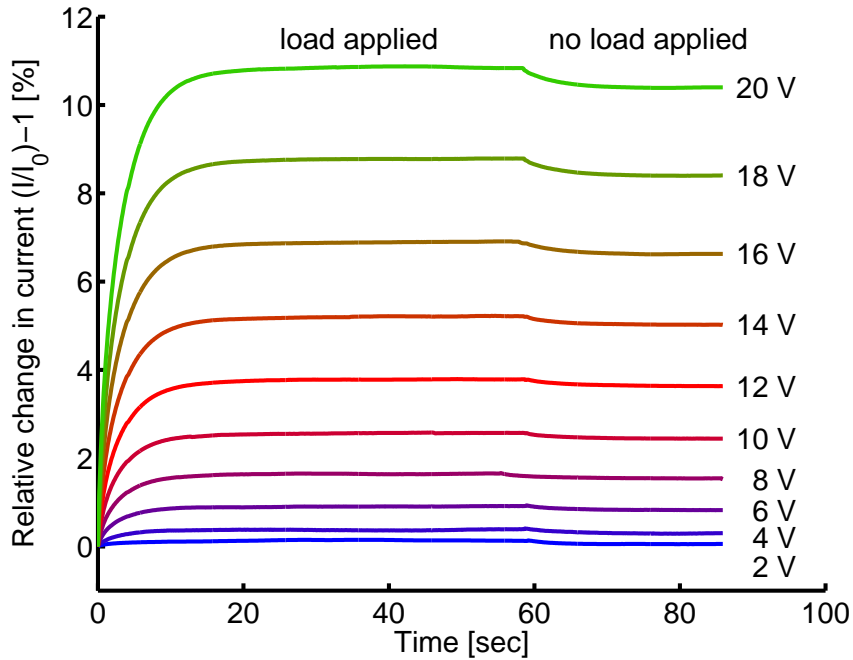


Figure 28: Relative current change through sample with 128 nm of Baytron® P on a 125 μm thick Kapton® substrate for different measurement voltages. The data points shown are relative values to the initial current before Joule heating shows effect and are calculated using $\Delta I_{\text{relative}} = (I(t) - I_{t=0})/I_{t=0}$ from the data of Figure 27

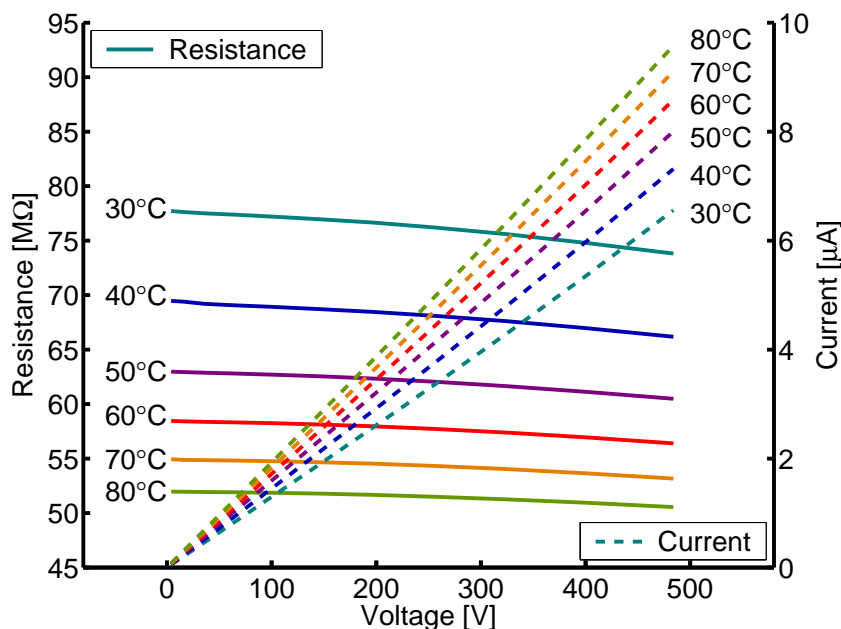


Figure 29: Selected data of current and resistance plotted as a function of voltage for different temperatures. The sample was made with a 42 nm thick layer of Baytron® P VP AI 4083.

3.5 Temperature dependencies

Temperature plays an important role in the charge transport of the organic conductive material investigated in this work. Not only the temperature dependence of the resistivity must be considered, but also the effect on the other material properties, such as the Young's modulus E .

3.5.1 Charge transport in PEDOT:PSS

To investigate the thermal dependencies of the used PEDOT:PSS films, some samples were characterized in a heating stage placed in the desiccator. Temperature sweeps were performed starting from room temperature up to 120°C. Sufficient time was given after setting each temperature value to uniformly heat up the sample, ensured by checking the resistance of the sample until it reached a stable value. For each temperature, the I-V characteristic of the resistor was recorded. As an example, selected measurement results are displayed in Figure 29 for a sample made from Baytron® P VP AI 4083. The collected data was then analyzed based on an appropriate model. Several theories to describe the charge transport in conducting polymers can be found in literature and some are described in the listed publications [47, 48, 46, 45].

The first approach was to approximate the measured values with the Gaussian Disorder Model

(GDM). The model was proposed by Borsenberger and Bäessler in 1990 [43, 44] to explain the charge transport in disordered molecular solids. The hopping mechanism is described by the jump rate and parameters for the mathematical model were found using Monte Carlo simulations. The final description of the mobility μ depending on the disorder parameters $\widehat{\sigma}$, Σ and the electric field E is given in equation 24. In Borsenberger's paper, a fit to experimental data is presented for samples made with 1,1-bis(di-4-tolylaminophenyl)-cyclohexane (TAPC) doped (Bisphenol-A-polycarbonate) (BPPC).

$$\mu(\widehat{\sigma}, \Sigma, E) = \mu_0 \exp \left[- \left(\frac{2}{3} \widehat{\sigma} \right)^2 \right] \times \left[\exp \left(C (\widehat{\sigma}^2 - \Sigma^2) \sqrt{E} \right) \right] \quad (24)$$

It was also observed that the disorder parameter Σ has a minimum value of 1.5. C is a constant with a value of $2.9 \times 10^{-4} \text{ (cm/V)}^{\frac{1}{2}}$. The energetic disorder parameter is defined by $\widehat{\sigma} = \frac{\sigma}{k_b T}$. T is the absolute temperature, k_b is Boltzmann's constant and σ is the standard deviation of the site energy assuming a Gaussian Distribution. As can be seen, the natural logarithm of the zero field mobility depends on $1/T^2$. The resistance R is proportional to the resistivity ρ (see equation 6) as long as the thermal expansion and thus a change in dimensions for the resistor can be neglected. The resistivity ρ is defined in equation 25 where the subscript n refers to electron transport while p indicates hole transport. For electron and hole conduction, q is the elementary charge e and has a value of $1.602 \times 10^{-19} \text{ C}$.

$$\rho = \frac{1}{q(\mu_n n + \mu_p p)} \quad (25)$$

Assuming that only the mobility μ depends on temperature and not the number of free carriers n or p and the transport of either holes or electrons is dominant, the resistivity $\rho(T)$ becomes proportional to $1/\mu(T)$. Since the change in dimensions of a resistor caused by the thermal expansion of the material can usually be neglected, the resistance $R(T)$ is a linear function of the resistivity $\rho(T)$ and thus also of $1/\mu(T)$. Therefore, for the GDM, a plot of $\ln(1/R)$ versus $1/T^2$ should result in a straight line. To cancel out the field dependence of the mobility stated in equation 24, the interpolated value of R for the E -field converging to zero ($E \rightarrow 0$) can be extracted from the measured I - V characteristics (see Figure 29). It was found out that this approach works better than just measuring the resistance at a low voltage. In Figure 30(a) the resulting $\ln\left(\frac{1}{R}\right)$ is plotted as a function of $\frac{1}{T^2}$ showing the data points close to a straight line expected for a linear dependence over the tested

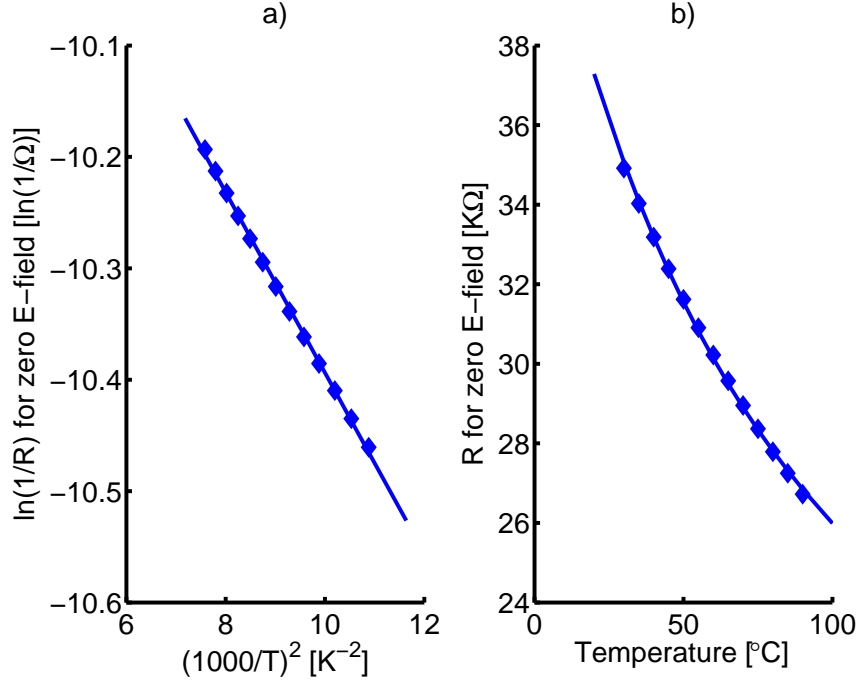


Figure 30: Thermal dependence of a resistor made with Baytron® P according to the Gaussian Disorder Model. a) $\ln(1/R)$ as a function of $(1/T)^2$ and b) R as a function of T for a resistor made with a 128 nm thick layer of Baytron® P. The dots are measured values while the solid lines represent curve fits following equation 28.

temperature range. Figure 30(b) displays the zero-field resistance as a function of temperature and the expected values according to the model described in equation 24 (solid line). The mobility depends also on the electric field E as is stated in equation 24. Measurements were done with different voltages resulting in different field-strengths for E . But the Joule heating effect shows much more impact on the current-voltage characteristic than the field dependence of the mobility. Therefore, a total evaluation to identify all parameters of the Gaussian Disorder Model was not possible. The energetic disorder coefficient σ was found to be approximately $6.1 \cdot 10^{-21} \text{ J}^{-1}$. Since the doping concentration is unknown, the zero field mobility μ_0 could not be evaluated.

Another approach was to investigate if the temperature dependence of the mobility follows an Arrhenius function. Blom and Vissenberg published a study about the charge transport in poly(p-phenylene vinylene) (PPV) in 2000 [39]. In their investigation, they observed that the mobility μ_p for this p-type material follows closely the empirical equation

$$\mu_p(E, T) = \mu_o \exp\left[-\frac{E_a}{k_b T}\right] \times \exp\left[B\left(\frac{1}{k_b T} - \frac{1}{k_b T_o}\right) \sqrt{E}\right] \quad (26)$$

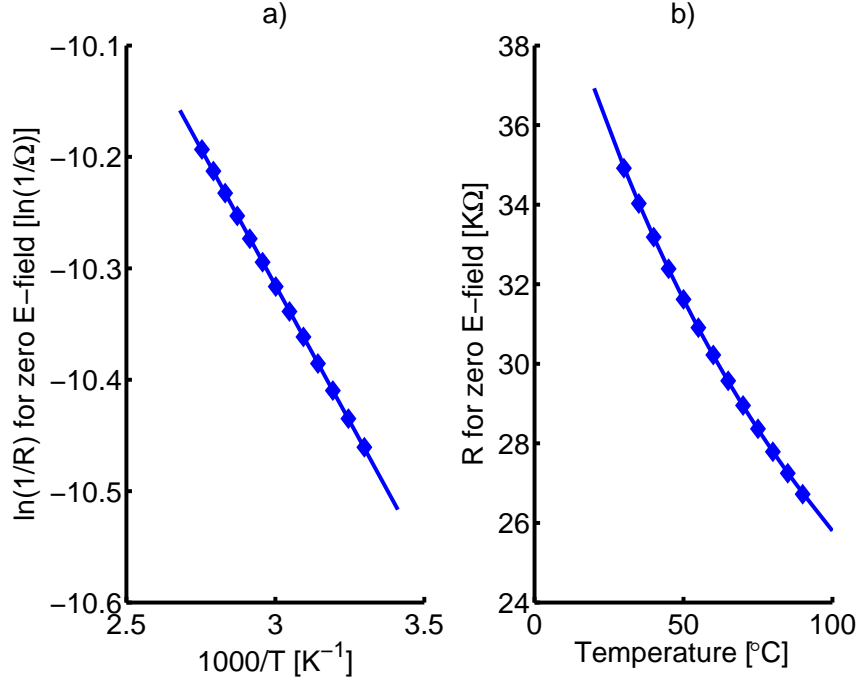


Figure 31: Thermal dependence of a resistor made with Baytron® P following an Arrhenius function. a) $\ln(1/R)$ as a function of $1/T$ and b) R as a function of T for a resistor made with a 128 nm thick layer of Baytron® P. The dots are measurement values while the solid lines represent curve fits following equation 26.

Here, the mobility depends on an activation energy E_a and the natural logarithm of μ_p is only a function of $\frac{1}{T}$. This empirical form of the mobility was also found in PVK and other disordered molecular materials. A physical derivation of this equation was not found yet. Thus, plotting the natural logarithm of the inverse of the zero-field resistance as a function of $\frac{1}{T}$, a straight line should result. If the values for the measured resistance from Figure 30 are plotted using this approach, a perfect linear dependence results as displayed in Figure 31. Extracted parameters for several measurements are summarized in Table 5. For the investigation of the piezoresistive effect, only the activation energy of the Arrhenius function is of interest. The impact of the field strength on the mobility is negligible and far smaller than the effect of Joule heating of the sample which depends on the voltage squared. The temperature dependence was investigated within the interval from 293 K to approximately 400 K because only a heating stage was available but cooling was not possible. Therefore, a curve fit can only be made over this limited range. Over this temperature range, the second model (mobility follows an Arrhenius function) seems to describe the measured values better

Table 5: Parameters for empirical model of mobility following an Arrhenius function for Baytron[®] P.

Sample	Activation energy E_a	Layer thickness of Baytron [®] P
1	0.0499 eV	128 nm
2	0.0422 eV	128 nm
3	0.0423 eV	63 nm
4	0.0335 eV	204 nm

than the first approach (Gaussian Disorder Model). To confirm this, a larger temperature range would have to be investigated.

Linearizing the resistance-temperature curve (see Fig 31(b), the temperature coefficient of resistance, α_T , can be extracted. Between 30°C and 90°C, α_T is $-3.5 \cdot 10^{-3} K^{-1}$ for the given sample. The magnitude of the value is close to those found in metals, but has opposite sign. The temperature dependent resistance $R(T)$ can be approximated by

$$R(T) = R_o (1 + \alpha_T \cdot \Delta T) \quad (27)$$

where R_o is the resistance at given reference temperature and ΔT the temperature offset from that reference.

The same approach used to describe the thermal dependence of samples from Baytron[®] P was chosen to identify the dependence of resistivity on temperature for Baytron[®] P VP AI 4083. A temperature sweep using the heating stage was performed with such a sample as well. The evaluation showed that the measured values could not be approximated by the Gaussian Disorder Model nor by an Arrhenius function. Therefore, a new empirical approach was pursued following

$$\mu_p(T) = \exp\left(-\left(\frac{E_a}{k_b T}\right)^q\right) \quad (28)$$

Analog to the data evaluation done for samples made with Baytron[®] P, the natural logarithm of $\left(\frac{1}{R}\right)$ was plotted against $\left(\frac{1}{T}\right)^q$. The least deviation to a linear curve fit in this representation was found for $q = 5.3$. Thus, $\ln\left(\frac{1}{R}\right)$ plotted as a function of $\left(\frac{1}{T}\right)^{5.3}$ should result in a straight line. Figure 32(b) displays the zero-field resistance as a function of temperature and the expected values according to the model described in equation 28 (solid line). The activation energy E_a was extracted from the measured data and is 0.0246 eV.

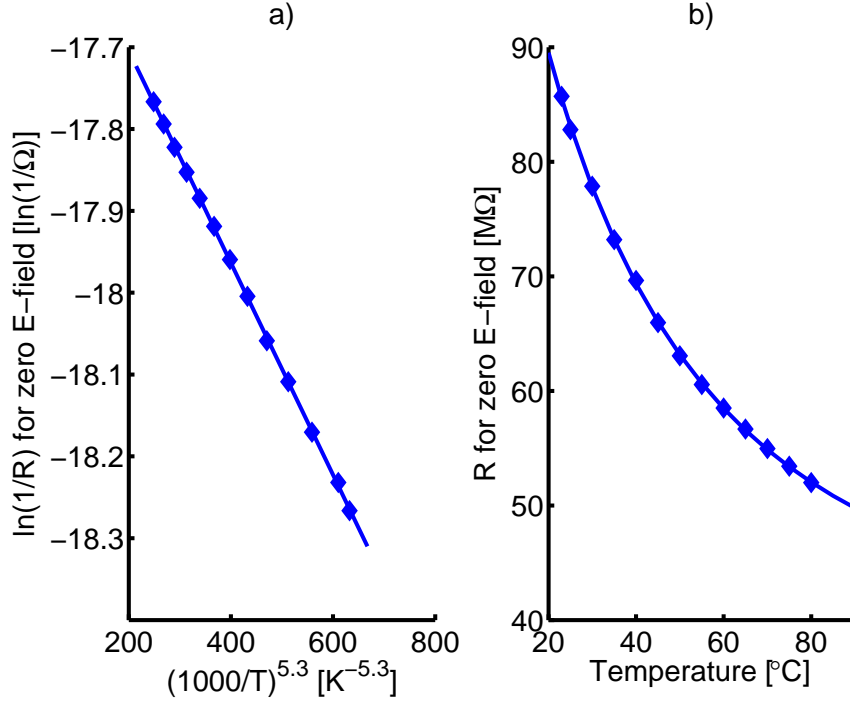


Figure 32: Dependence of a) $\ln(1/R)$ on $(1/T)^{5.3}$ and b) R on T for a resistor made with a 42 nm thick layer of Baytron® P VP AI 4083. The dots are measured values while the solid lines represent curve fits following equation 28.

3.5.2 Thermal impact on substrate material

To evaluate the piezoresistive effect obtained from measurements with changing loads to a sample, the material properties of the substrate must be known. Since the effect is investigated for different temperatures, the dependence of the elastic modulus E on temperature have to be considered. To this end, the supplier of the Kapton® material, DuPont®, made data available measured for the type 500 HN foil used in the experiments (see Figure 33). For the following evaluations, linearly interpolated values based on these data points are used for the Young's modulus E .

Since Kapton®, the material used as a substrate, is not purely elastic but visco-elastic, the strain caused by an external load is not fully reversible but may lead to a plastic deformation. The effect is known and referred to as creep [86]. For small strains and at temperatures far below the glass transition temperature of the plastic substrate, the effect is negligible. At elevated temperatures and for high loads, the effect has to be considered. Creep is a serious issue especially for sensor applications. It will cause a drift in the output signal for a constant static load. An investigation of the

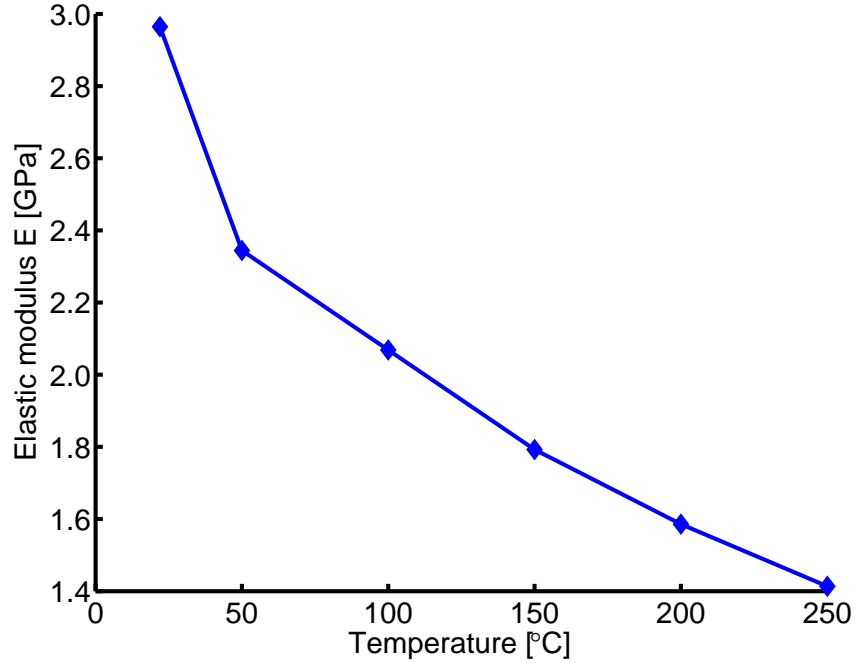


Figure 33: Elastic modulus E of Kapton® 500 HN as a function of temperature. [Measurements courtesy of DuPont]

visco-elastic behavior of Kapton® polyimide foil can be found in [78]. Data therein is summarized for different stresses and temperatures.

In the present work, the resistance of a sample was recorded over several hours with different static loads to investigate the effect. The measurement data is presented in Figure 34. Since the resistor material is almost stable under inert gas conditions, a change in resistance must be caused by an increase in strain in the substrate material. A constant voltage of 80 V has been applied for all measurement cycles. Due to the Joule heating effect, the temperature of the sample was elevated. The exact value was not measured but can be estimated to be in the range of 60°C to 70°C. While a quantitative conclusion cannot be derived, an increasing load results in a stronger drift of the resistance signal, indicating creep in the substrate at elevated temperatures. To strengthen the qualitative explanation, the measurements were repeated with a pulsed measurement voltage with low duty cycle (two seconds every minute). The Joule heating effect is negligible in that case since the averaged power consumption is reduced by a factor of thirty. For these measurements, no change in resistance was observed over a sixteen hour measurement period with applied load of 1 kg (see Figure 34, dashed line). The sample had a width of 2 mm and the thickness of the Kapton®

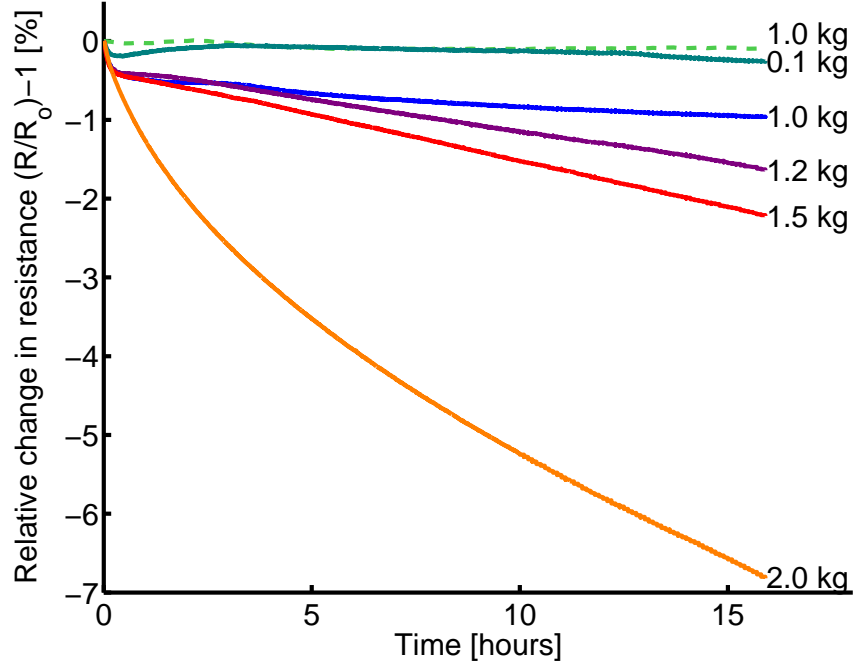


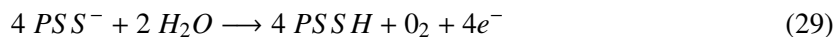
Figure 34: Drift in measured resistance value caused by creep of the Kapton® substrate. Displayed is the relative change of the resistance ($\Delta R/R = (R(t) - R_{t=0})/R_{t=0}$) of a sample resistor as a function of time and subject to constant loads. Due to Joule heating the temperature was elevated to estimated 60°C to 70°C for all measurements represented with solid lines. Data for the one dashed curve was taken at room temperature.

substrate is $125\ \mu\text{m}$. For the estimated temperature range of 60°C to 70°C , the elastic modulus can be extracted from Figure 33 and the calculated elastic strain at elevated temperatures for the maximum load of $2\ \text{kg}$ is approximately $3.3\ \%$. Assuming that the change in resistance is solely due to a piezoresistive effect, the strain caused by creep of the sample can be calculated if the gage factor is known. For this sample, a gage factor of approximately -0.34 was identified for the estimated temperature range and a strain of approximately 5% after 12 hours with a load of $1.5\ \text{kg}$ (stress of $58\ \text{MPa}$) was calculated therewith. This value is higher compared with data from literature [86], where the creep of Kapton® under similar stress ($60\ \text{MPa}$) but higher temperature (100°C) after 12 hours is approximately 1% . Qualitatively, the shapes of the curves when the strain is plotted as a function of time look alike. Also, it is stated that the polyimide is not linearly viscoelastic since as stress is doubled, the amount of creep is more than doubled [86]. The same observation was made in the present work. In the reference, the type of Kapton® foil and the dimensions of the sample are not specified.

3.5.3 Thermally activated de-doping

For measurements with high power dissipation and thus strong Joule heating, a thermal runaway process was observed. Since the sample resistance decreases with rising temperature, the power consumption is increasing and therefore causing a higher Joule heating effect. Once a critical value is passed, this positive feedback leads to a fast heating of the sample until it 'fuses'. A typical measurement curve is shown in Figure 35. For comparison with the measurements below the critical value, two curves recorded at lower voltages are given as well. For small applied voltages, the current increases after turning on the voltage at $t = 0$ until the sample has thermally stabilized. For $V = 120\text{ V}$, the positive feedback results in a strongly increasing current which is eventually limited from the measurement device. In the experiment, the maximum current was set to 2.5 mA (300 mW power dissipation). After 108 seconds, the current suddenly drops, i.e. the resistance has drastically increased. This rise in resistance is not caused externally but results from an internal change of the resistor material.

The effect can be utilized to build memory devices as described by Möller et al. [87, 82]. There, PEDOT:PSS is deposited between a silicon diode and a metal electrode. With a voltage applied in the forward direction of the diode, the conductive polymer will 'fuse' and increase in resistance. When only small voltages are applied, the resistivity can be read out without causing a change in resistance. Built as an array with multiple single devices, a 'write once - read many times' memory (WORM) can be fabricated. The use of the diodes allows addressing single elements by selecting row and column of the array which represent lines of bottom and top contacts respectively. The reported change in resistance is up to a factor of 1000. A characterization of the effect is given as well as an explanation of the transition from high to low conductivity as follows: The charged sulfonate groups (SO_3^-) of PSS can be stabilized by hydrogenation to PSSH via the chemical path:



Since the PSS is transferred to a neutral state, the PEDOT becomes undoped, or at least loses its high doping level. The chemical reaction is a thermally activated process. In the evaluation of Möller et al., the temperature level required for the chemical reaction described in 29 was calculated to be approximately 200°C . This is consistent to observations made on Joule heated samples in the

present work. The temperature peak measured with an infrared camera from a sample 'fused' in air was in the range of 170°C to 190°C . Although equation 29 includes the presence of water, the effect of thermally activated de-doping was also observed in samples characterized under nitrogen. Possibly even small amounts of H_2O are sufficient as from the remaining humidity in the inert gas atmosphere or from water absorbed into the film and substrate material. The increase in resistance resulting from 'fusing' was approximately 440 in the present work. Within limits, the film was stable afterwards. For measurements with very high voltages ($> 350\text{ V}$) and resulting high power consumption, the current became unstable. Eventually, the samples were physically destroyed. During this final destruction process, sparks were observed and the sample resistor became irreversibly insulating.

Another hint is the observation that the resistance of an externally heated sample is decreasing with temperature up to approximately 100°C . Above 100°C , the resistance increases with temperature and therefore some other effect must have been triggered. The chemical degradation of PEDOT starts at 150°C as reported by Kiebooms et al. [88]. PEDOT films tested in their study were prepared by anodic oxidation and doped with PF_6 . Major film decomposition occurs in the region between 390°C and 450°C .

Chemically de-doped PEDOT films were investigated by Johansson and co-workers [37]. One result shows that it is difficult to obtain undoped material at all, since the neutral polymer is highly sensitive to oxygen and will be re-doped spontaneously in air. With an in-situ approach using electrolytes (see also chapter 1.2 of the present work) it was found out that the conductivity decreases by 4-5 orders of magnitude when the PEDOT material is completely de-doped.

3.6 Piezoresistivity found in PEDOT:PSS

To determine the piezoresistive effect in PEDOT:PSS thin films, samples made with Baytron[®] P VP AI 4083 and Baytron[®] P were investigated. They were stretched with defined loads and the change in resistance was recorded. For different measurement voltages not only the electric field and the current changes but also the temperature of the samples due to Joule heating. The actual temperature could not be measured directly since the characterization was done in a closed desiccator flushed with nitrogen. But using the theoretical models described in chapter 3.5.1, the

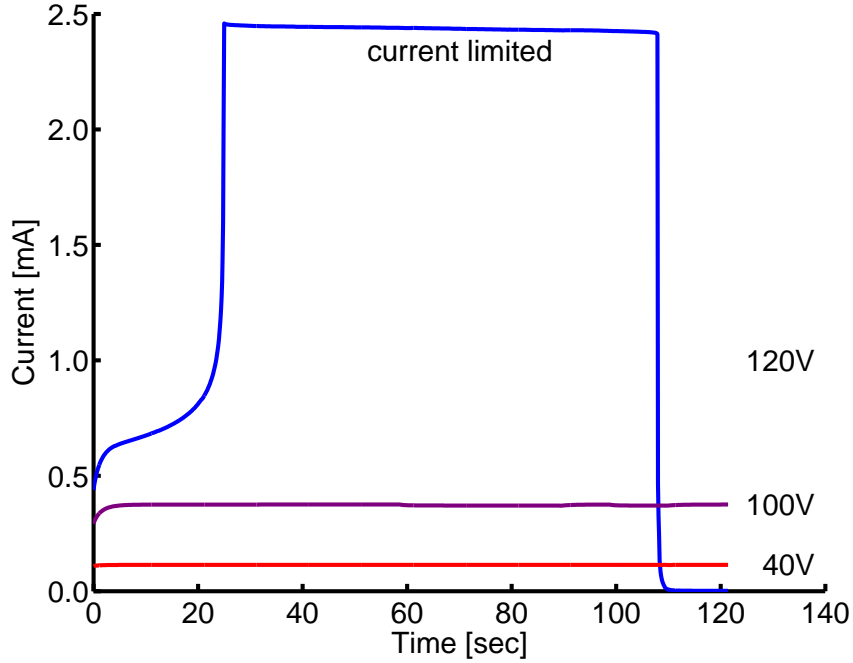


Figure 35: Current measurements from a thermal runaway process due to decrease in resistance with rising temperature. For this sample, the critical power was reached at 120 V. At about 2.5 mA the current is limited from the measurement equipment. After 108 seconds the current drops.

temperature could be determined out of the resistance change due to Joule heating only. Samples from Baytron® P followed closely an Arrhenius function and the activation energy was determined by heating-experiments with a hot plate as described in section 3.5.1. Since the resistance without the self-heating effect at the beginning of each measurement cycle as well as the ambient temperature are known, the actual mean temperature of the sample can be calculated from data shown e.g. in Figure 27. Three important values can be extracted from such a measurement cycle:

First, the current is recorded at $t = 0$, just after the voltage was applied. It will be named $I_{0, RT}$. In that state, the sample is approximately at room temperature, which is measured with a thermometer in the desiccator. Second, the current after it stabilizes before the load change is done ($t = 45 - 50 \text{ sec.}$) has to be noted. At this point, the sample is at elevated temperature due to the Joule heating. Note that a weight is attached to the sample in the first part of the measurement cycle, thus it is strained. Therefore, the current will be labeled $I_{strained, warm}$. After the load is lifted ($t = 58 \text{ sec.}$) from the sample, the current changes again, which can be seen best if displaying relative current changes (see Figure 28). Again, it takes several seconds until the current is stabilized

($t = 75 - 85 \text{ sec.}$). The average current at this point will be termed $I_{unstrained, warm}$. The currents $I_{strained, warm}$ and $I_{unstrained, warm}$ are averaged over several seconds to reduce the noise.

Out of this data, the average temperature of the sample can be calculated as well as the actual change in resistance due to the load change. The following evaluation scheme was used for the measurements taken from Baytron® P samples. According to the model following an Arrhenius function as described in section 3.5.1, the dependence of the resistance on temperature can be described with two parameters, the activation energy E_a and the resistance R_o

$$R(T) = \frac{R_o}{\exp\left(-\frac{E_a}{k_b T}\right)} = R_o e^{\left(\frac{E_a}{k_b T}\right)} \quad (30)$$

The activation energy is assumed to be constant and was identified with reference measurements. A value of $E_a = 0.042 \text{ eV}$ was used for the following calculations, which is the mean of the data summarized in Table 5. The value for R_o can then be determined with one known resistance value taken at a known temperature for each sample, following equation 31.

$$R_o = R(T) \exp\left(-\frac{E_a}{k_b T}\right) \quad (31)$$

The calculation of R_o was based only on the first measurement of a new series for each sample. Since the next cycle with increased voltage was usually done within two to three minutes, the sample might still have had an increased temperature due to the self-heating effect from the previous measurement. At room temperature, $R(T)$ is then $V/I_{0, RT}$. With the known activation energy and R_o , the average temperature of the sample can be calculated from any measured resistance, as long as the sample remains in the same condition. Thus, since the reference resistance R_o is determined with the resistor strained, the sample has to be stretched with the same load to allow the calculation of its temperature at any other time. Equation 30 rearranged to solve for the temperature gives

$$T = -\frac{E_a}{k_b} \ln\left(\frac{R(T)}{R_o}\right) \quad (32)$$

The resistance $R(t)$ is calculated using $R(T) = V/I_{strained, warm}$. With the known temperature T , calculated from equation 32, the adequate elastic modulus E can be found as described in section 3.5.2 and using Figure 33. Knowing E , the effective strain ϵ of the sample can be computed depending on the attached weight.

When the load on the sample is removed after approximately one minute the resistance shifts. The relative change of resistance is given by

$$\left[\frac{\Delta R}{R} \right]_{measured} = \frac{R_{strained, warm} - R_{unstrained, warm}}{R_{unstrained, warm}} \quad (33)$$

Using this definition, a positive sign for $\left[\frac{\Delta R}{R} \right]$ indicates an increase in resistance when the sample is strained. The change in resistance is due to a change in geometry and the piezoresistive effect. Chapter 1.4.3 includes the appropriate equations to describe the geometrical and the intrinsic piezoresistive effect. Altering the sample geometry also affects the effective thermal resistance of the sample and thus its average temperature. The Joule energy released in the active resistor area is transported along the support to the clamping. It is a justified assumption that heat conduction is the dominant transfer mechanism as described in section 3.4. In equation 22, the dependence of a temperature increase on generated power and geometrical conditions is given. A change in temperature will also cause a change in resistivity and thus in the resistance of the sample. The effects will superimpose to one measurable change in resistance

$$\left[\frac{\Delta R}{R} \right]_{longitudinal, measured} = \underbrace{(1 + 2\nu)\epsilon}_{geometrical} + \underbrace{\pi_l \cdot E \cdot \epsilon}_{piezoresistive} + \underbrace{\left[\frac{\Delta R}{R} \right]_{th}}_{thermal} \quad (34)$$

To determine the magnitude of the piezoresistive coefficient π_l , the change in resistance due to the new thermal conduction conditions has to be calculated. The derivation is analogue to the one for the geometrical effect on resistance (see chapter 1.4.2) by replacing the dimensional variables in equation 22 with the stretched ones.

$$\Delta T = \frac{l}{\sigma_{th} \cdot A} P (1 + \epsilon (1 + 2\nu)) \quad (35)$$

The difference in temperature rise $\partial \Delta T$ between the strained and unstrained sample is thus

$$\partial \Delta T = \epsilon (1 + 2\nu) \Delta T = \frac{l}{\sigma_{th} \cdot A} P (1 + 2\nu) \epsilon \quad (36)$$

and is the source of an additional, thermally generated resistance change. The thermal conductivity σ_{th} along the support as well as the dimensions l and A are constant for a given sample. C is constant for each sample as defined in equation 37 and its value can be found by plotting the determined temperature values as a function of the dissipated power in the resistor as shown in Figure 36. A

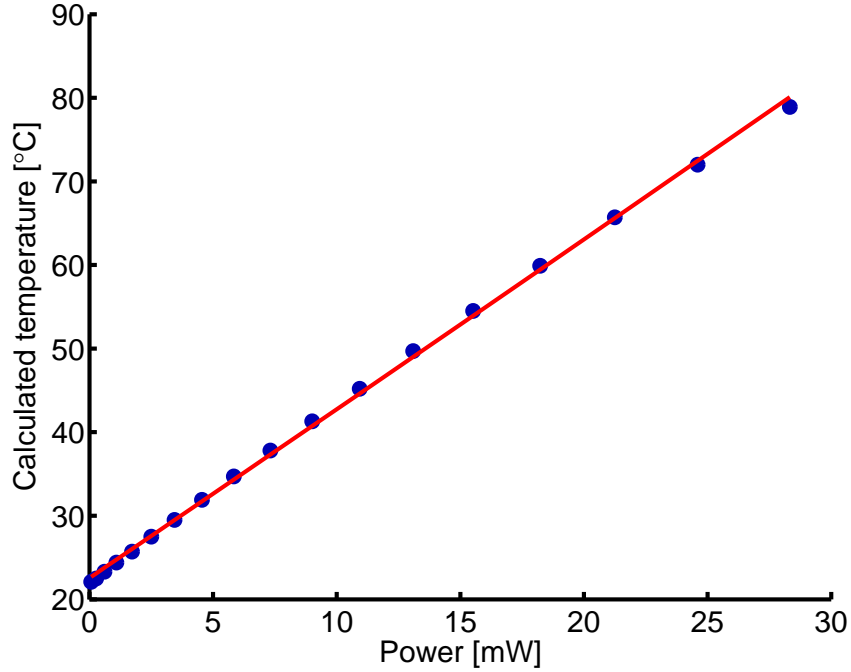


Figure 36: Experimental temperature values determined from measurements at different voltage as function of the dissipated power. Data is shown for a sample with a 48 nm thick layer of Baytron® P (dots). The solid line is a linear fit.

straight line is expected with a slope equal to C .

$$C = \frac{l}{\sigma_{th} \cdot A} \quad (37)$$

To calculate $\partial\Delta T$, this constant C is used together with the heating power P for the unstressed resistor calculated by $P = V \cdot I_{unstrained, warm}$. The resulting resistance change caused by a small change in temperature of a thin film resistor cast from Baytron® can be found by linearizing equation 30. With the assumption that the temperature change $\partial\Delta T$ is much smaller compared to the actual temperature T , the following definition is obtained:

$$\left[\frac{\Delta R}{R} \right]_{th} = - \frac{E_a}{k_b T} \cdot \frac{\partial\Delta T}{T} \quad (38)$$

In case of low power consumption and therefore small Joule heating, the effect is negligible since it is dependent on power P . For a strong self-heating effect leading to much increased temperatures of the sample, it should be taken into account. The contribution of the geometrical, the intrinsic piezoresistive and the thermal effect on the measured change in resistance $\Delta R/R$ at different temperatures of a sample with a 48 nm thick layer of Baytron® P is summarized in Table 6. The effective

Table 6: Measured change in resistance of a thin film resistor from Baytron® P split by origin for different temperatures. Evaluation is for a sample with a 48 nm thick layer of PEDOT:PSS.

Sample temperature	Dissipated power	Measured gage factor $GF = \frac{\Delta R/R}{\Delta l/l}$	Contribution to GF $\left(\frac{\Delta R/R}{\Delta l/l}\right)$ caused by		
			geometrical effect	piezoresistive effect	thermal effect
24.3°C	1.1 mW	-0.015	+1.680	-1.674	-0.020
49.7°C	13.1 mW	-0.187	+1.680	-1.657	-0.209
72.0°C	24.8 mW	-0.361	+1.680	-1.695	-0.346
95.3°C	37.5 mW	-0.564	+1.680	-1.782	-0.462

resistor area is 1.87 mm^2 ($w=1.7 \text{ mm} \times t=1.1 \text{ mm}$) and with a 1 kg load the maximal strain at 95.3°C is approximately 2.2 %. The geometrical piezoresistive effect is positive and depends on temperature only because of the dependence of the Young's modulus on temperature, which is not noticeable in the representation chosen for Table 6. It is also assumed that the Poisson's ratio ν for the substrate is not a function of temperature. Both, the thermal effect and the intrinsic piezoresistive effect are negative and increase in magnitude with increasing temperature. Since the geometrical and the intrinsic effect are close in absolute value but of opposite sign, they partially cancel each other out, resulting in a small measured gage factor ($|GF| < 1.1$ for all measured samples). Considering all three effects, the look of the plotted current as a function of time for a typical measurement cycle shown in Figure 21 can be explained. The load to the sample has been removed after 28 seconds resulting in a small peak of the current. This increase is due to the geometrical effect though reduced in magnitude by the superposition of the piezoresistive effect but still positive in sign. Directly after the load change, the thermal effect does not contribute since heat conduction is not instantaneous but a time dependent process. Within the next seconds, the current is decreasing which is a result of the temperature dropping because of the better heat conduction in the unstressed state.

Following the presented analysis, all variables of equation 35 are known apart from the piezoresistive coefficient π_l which can now be evaluated from the measurement data for different temperatures. The results for several samples of thin film resistors from Baytron® P are shown in Figure 37. Although the values fluctuate around the overall linear curve fit, the general dependence of the

piezoresistive effect on temperature is consistent for all samples. Measurement errors of the geometric dimensions of the samples or from an error in the initial resistance value used to determine the sample temperature might cause the offset from the averaged linear curve fit.

To calculate the transverse piezoresistive coefficient π_t from the measurement data, the same approach was used. The description of the geometrical effect has to be changed according to the derivation given in chapter 1.4.3, while the calculation of the thermal effect is the same. In Figure 38, the extracted values as a function of temperature are displayed. The coefficient π_t is opposite in sign to the longitudinal coefficient π_l . Since the strain in x- and y-direction is linked by the Poisson effect, such a behavior is expected for anisotropic material. Its magnitude at room temperature is about two third of the one describing the longitudinal effect.

The same evaluation was done for the measurement data taken on samples with Baytron® P VP AI 4083. For the temperature compensation, the empirical model described in section 3.5.1 was used. Since the resistivity of this type of PEDOT:PSS is much higher, the power consumption is lower and so is the Joule heating. The limitation in power was due to the measurement equipment, as the maximum measurement voltage is 500 V. Therefore, the evaluation could only be done for a temperature range between 20°C and 60°C. A considerable higher noise level was observed in the current measurements on these samples. In Figure 39, the extracted longitudinal piezoresistive coefficient is presented and in Figure 40, the transverse piezoresistive coefficient is displayed. The values extracted for thin film resistors from Baytron® P and Baytron® P VP AI 4083 are of the same order of magnitude. The piezoresistive coefficients π_l and π_t follow the same temperature dependence, thus increasing in magnitude with rising temperature.

Sirringhaus and his co-authors demonstrated that the alignment of polymer chains in direction of the current plays an important role in device performance [89]. In their work, a polymer field effect transistor based on a polyfluorene copolymer has been optimized. The material was spin-coated on an alignment layer (a mechanically rubbed polyimide) resulting in a film with oriented chains. Mobility anisotropies of 5-8 for current flow parallel and perpendicular to the alignment direction were measured. Sirringhaus et al. also present a mathematical model predicting the anisotropy based on the geometrical aspects. Another approach to increase the mobility in conductive polymers by

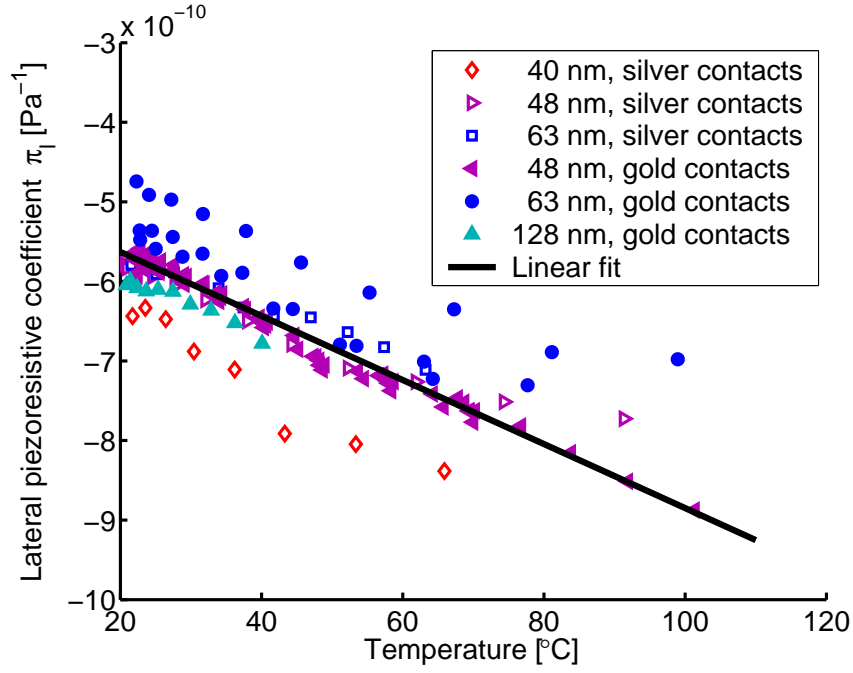


Figure 37: Longitudinal piezoresistive coefficient π_l for Baytron® P as a function of temperature. The values given in the legend are the thicknesses of the PEDOT:PSS layer. The overall linear curve fit (solid line) was evaluated for all samples between 20°C and 70°C.

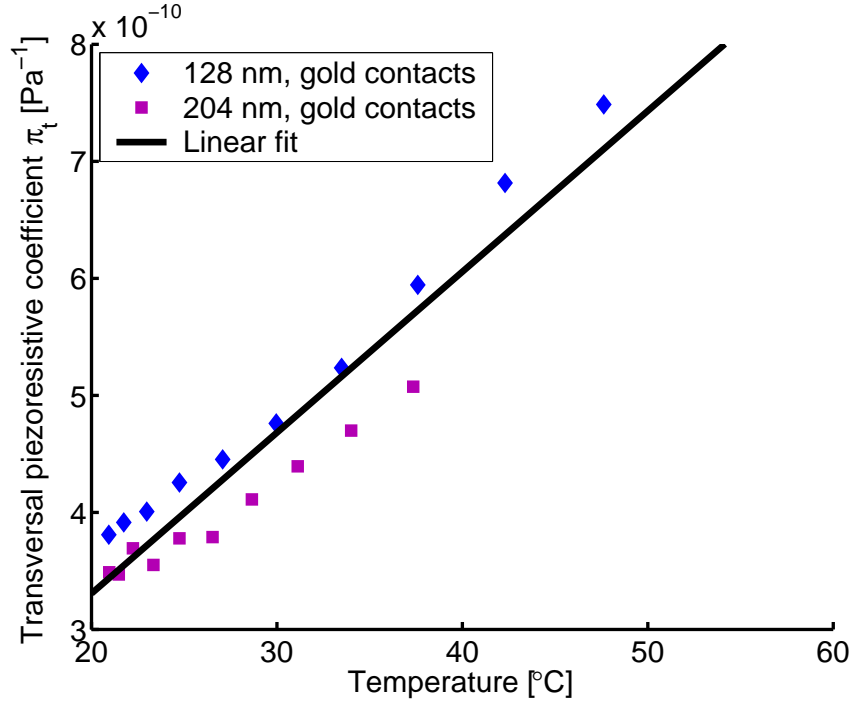


Figure 38: Transverse piezoresistive coefficient π_t for Baytron® P as a function of temperature. The values given in the legend are the thicknesses of the PEDOT:PSS layer. The overall linear curve fit (solid line) was evaluated for all data points.

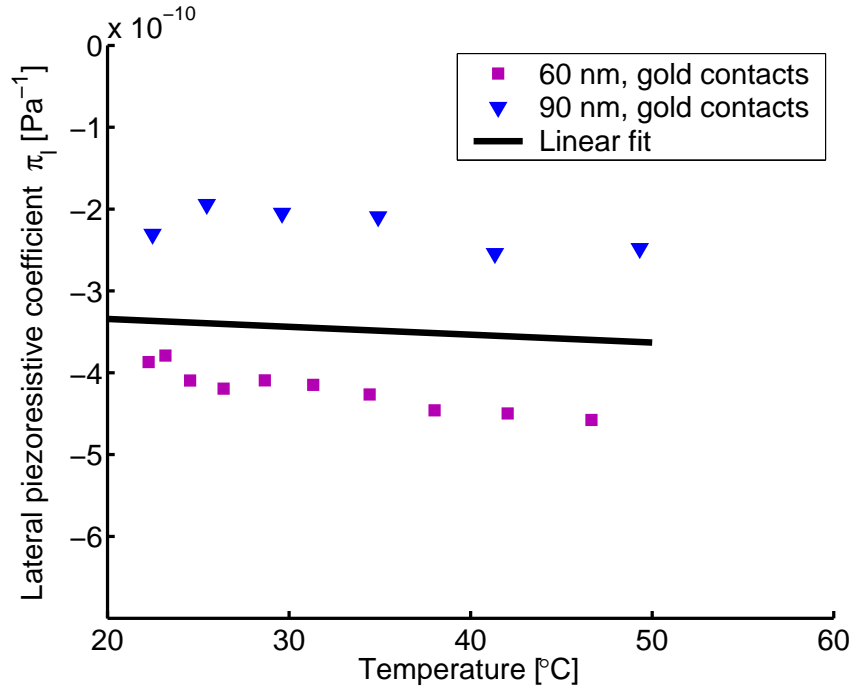


Figure 39: Longitudinal piezoresistive coefficient π_l for Baytron® P VP AI 4083 as a function of temperature. The values given in the legend are the thicknesses of the PEDOT:PSS layer. The overall linear curve fit (solid line) was evaluated for all data points.

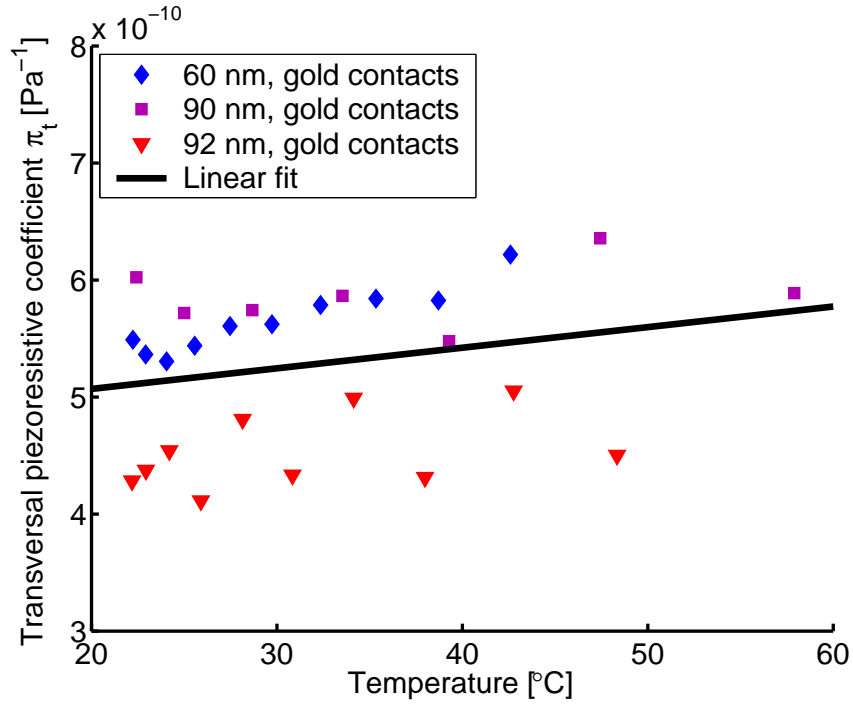


Figure 40: Transverse piezoresistive coefficient π_t for Baytron® P VP AI 4083 as a function of temperature. The values given in the legend are the thicknesses of the PEDOT:PSS layer. The overall linear curve fit (solid line) was evaluated over all data points.

aligning the chains is reported in [90]. Thin films of undoped polythiophene in a field effect transistor configuration, supported on polyethylene, were stretch-oriented to a maximum of 4.5 times the original length. The anisotropy in mobility reached values up to 4. Based on these observations, a negative longitudinal piezoresistive effect in conductive polymers which consist of entangled, long polymer chains can be explained as follows: The conductivity along a doped chain is high because of the presence of delocalized electrons from the π -conjugated structure. Limitations result rather from hopping from one conjugated polymer chain segment to another than from current flow along the chain. Hopping to a chain aligned in the same direction is much easier than hopping to one perpendicular [89]. Thus, the better the polymer chains are aligned in the direction of the current flow, the lower the total resistance will be. In an amorphous, unstretched film, the polymer chains are distributed randomly. Once the film is stretched, the polymer chains will shift in position. They are pulled apart in the direction of the applied stress and pushed closer together in the perpendicular direction due to the Poisson effect. For a polymer piezoresistor with an applied stress in the direction of the electric field (longitudinal), the polymer chains are oriented more parallel in the direction of the current flow and therefore the resistance is decreased. In a transversal configuration, the polymer chains are also oriented more parallel in the direction of an applied stress, but in this case the direction is perpendicular to the current flow and thus the resistance of the material is increased. Since the anisotropy in mobility is not high and the change in orientation as a result of a small strain of the polymer thin film is low as well, the resulting piezoresistive effect is small in magnitude.

The temperature dependence of the observed piezoresistive effect in PEDOT:PSS is either due to the thermally assisted hopping process or due to the fact that the polymer chains can move more easily and align themselves better at higher temperatures. Since the Joule heating effect was used for the thermal characterization, an increase in temperature implies an increase in power and also voltage. Therefore, the electric field is stronger at higher temperatures. Nevertheless, the piezoresistive effect rather depends on the temperature than on the electric field. Otherwise, the piezoresistive coefficient would change with the layer thickness of the conducting polymer based on the evaluation method described above. But not even a tendency for such a behavior was found as can be seen in Figure 37.

Piezoresistivity in samples with a degraded ('fused', as described in section 3.5.3) PEDOT:PSS

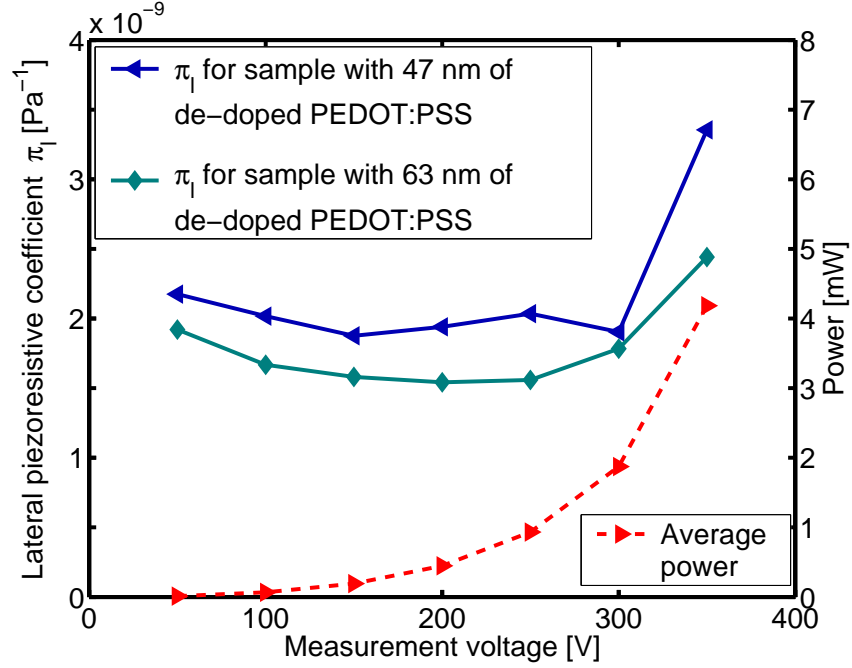


Figure 41: Longitudinal piezoresistive coefficient π_l for 'fused' samples from Baytron® P as a function of applied voltage.

layer was also investigated. The extracted piezoresistive coefficient in longitudinal direction, π_l , was calculated for measurements done at different voltages and is shown in Figure 41. Reference measurements to determine the temperature effect on the resistivity of the degraded films were not performed. Therefore, the temperature dependence of the piezoresistivity could not be determined. Instead, the power is plotted into the same graph. Since the temperature is almost proportional to the power, tendencies can be identified even though the magnitude cannot be evaluated accurately. The piezoresistive effect is positive for these samples and about three times higher in magnitude than for the initial film made from Baytron® P. Since the direction does not oppose the geometrical effect in this case, the actual change in resistance is even more pronounced. The resulting gage factor is approximately 7 and thus higher than the gage factor found in most metals.

3.7 Migration of silver ions in PEDOT:PSS

During the measurements on samples of Baytron® P VP AI 4083 with silver electrodes, an unexpected discovery was made. While investigating the long term stability in air, it was observed that



Figure 42: Microscope image of migrated silver on PEDOT:PSS resistor. A DC-voltage of 500 V was applied for 3 hours before the picture was taken. The anode is to the right.

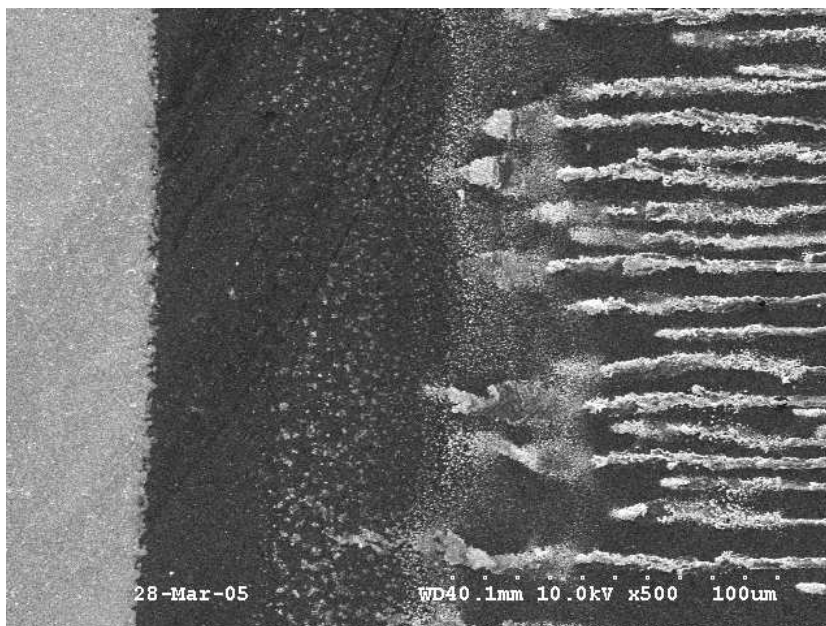


Figure 43: SEM picture of grown silver features on PEDOT:PSS resistor. The cathode is seen on the left side.

the resistance does not increase over time but decreases. This effect was not found in other samples with either gold electrodes or those which were tested under inert gas atmosphere. Using a microscope, a degraded anode and the formation of branch-like features on the resistor can be seen (Figure 42). The silver anode looks degenerated, while there is hardly a change in appearance on the cathode side. A better image of the 'grown' features is obtained by using a Scanning Electron Microscope (SEM) (see Figure 43). To ascertain the chemical components of these evolved branches, the Energy Dispersive X-ray (EDX) equipment of the SEM was used. The result showed that silver atoms must have been transported from the electrodes onto the PEDOT:PSS film. The transport of material can be of ionic nature alone. A possible reason why the effect is only observed in air is the presence of water in form of humidity under ambient conditions. PSS is acidic with chemical active

SO_3H groups. Together with H_2O and in contact with the silver electrodes, SO_3^- and Ag^+ -ions can form. The hydrogen either dissipates as H_2 or is built into the structure of the PEDOT molecule similar to the doping effect with PSS (see chapter 1.3.3). Ag^+ , the positive silver ions, are drifting from the anode to the negative cathode. The branched structure results from the fact that a highly conductive path is formed whenever a silver ion reaches the cathode or an already grown extend of it. Especially at the edges of the electrodes or wherever the electrodes were not straight and parallel to the current, it was obvious that the silver branches grew along the field lines, always perpendicular to the metal brink. The resistor length for the samples showing this effect were in the range of 1 mm to 4 mm. In the present work, the reversibility of the effect was not investigated yet. A similar effect leading to the formation of a conducting path from silver ions is utilized for a memory cell built as a sandwich structure with silver, silversulphide (Ag_2S), silver (very thin, 1 nm thick) and a platinum electrode on an insulating substrate [91]. Depending on the polarity of an applied voltage, the thin silver layer between Pt and Ag_2S is dissolved into the sulphide or forms a conductive bridge to the silver cathode. The function of the device is based on the special properties of Ag_2S that can transport both, electrons and ions, at room temperature.

CHAPTER IV

CONCLUSIONS AND OUTLOOK

Out of the various measurements taken from different samples of PEDOT:PSS resistors, several conclusions can be drawn. Some observations might still be unexplained and require further investigation.

4.1 Piezoresistivity found in PEDOT:PSS

PEDOT:PSS is considered an organic metal because of its high conductivity. In fact, there are more similarities. It was found out that the magnitude of the temperature coefficient of resistance, α_T and the magnitude and thermal dependencies of the piezoresistive coefficients π_l and π_t are comparable between metals and the electrochemically doped conjugated polymer. The difference is that all these effects are opposite in sign. The resistance in metal is increasing with temperature, while the investigated metallic polymer has a negative temperature coefficient. Both conductors have small longitudinal piezoresistive coefficients, but with positive sign for metals and negative sign for PEDOT:PSS. Also, for metals the piezoresistive effect decreases with temperature but for the conjugated polymer it is increasing.

An organic, conductive material was investigated to find out if it can be utilized as the sensing layer in force sensitive devices. PEDOT:PSS in its primary state exhibits a small, negative piezoresistive effect. The measurable change in resistance in response to an applied stress is partially canceled out by the geometrical effect, resulting in a gage factor of approximately -1.1 to $+0.3$ which is smaller in magnitude than that of typical metals ($GF = 2$ to 5). Thus, it cannot be recommended to use this material as of force sensitive layer.

The properties change after the material undergoes a transition induced by heating and irreversibly increasing its resistance ('fusing'). Then, the piezoresistive behavior shows a positive effect with a resulting gage factor of approximately 7 . Although the resistance is stable in this state, the usability is limited by the high resistivity of the material of approximately $2000 \Omega \text{ cm}$. Thus, it is

difficult to built in-plane thin-film resistors out of this material with resistances in the $K\Omega$ -range as desired for sensor applications. Furthermore, the reproducibility of the de-doping process has not been investigated yet.

It is believed that the origin of the piezoresistive effect lies in the dependence of the conductivity on the alignment of the chains in conjugated polymers. In a spin cast thin film, the molecules are distributed randomly, at least in the two in-plane directions. If the material is stretched, the polymer chains are arranged more parallel in the direction of the applied stress, resulting in a decrease of resistivity in longitudinal direction.

4.2 Further investigations

The change of resistance resulting from an applied stress perpendicular to the thin film was not investigated. For the given structure with the resistor formed in plane, only a small change in resistance is expected because the response of the polymer would not change much in comparison to the devices investigated in the present work. The polymer chains might be aligned more parallel when the thin film is compressed, in a similar way as the thin film is believed to behave under in plane stress. A sandwich structure with the PEDOT:PSS layer embedded between two metal electrodes might perform differently. A mobility anisotropy in thin films of conjugated polymers is reported in [89]. Although, materials with high resistivity can be used since the w/l -ratio is now much larger because the thin film thickness would be equal to the resistor length. But as long as there is no change in the conduction mechanism, only small variations of the observed piezoresistive effect are anticipated. Probably the 'fused' material can be utilized in a stacked structure to compensate for its high resistivity after the de-doping. The magnitude of the observed gage factor exceeds that of typical metals and because it can be solution processed it might be of advantage in the application of strain sensitive sensors.

The strong piezoresistive effect in single crystal silicon is caused by a change in the band structure when the lattice is subject to mechanical stress [2]. A similar effect might be found in highly ordered organic semiconductors. Thus, the investigation of materials with different thin film morphology might be fruitful. Oligomers and small molecules can form crystalline structures. Their

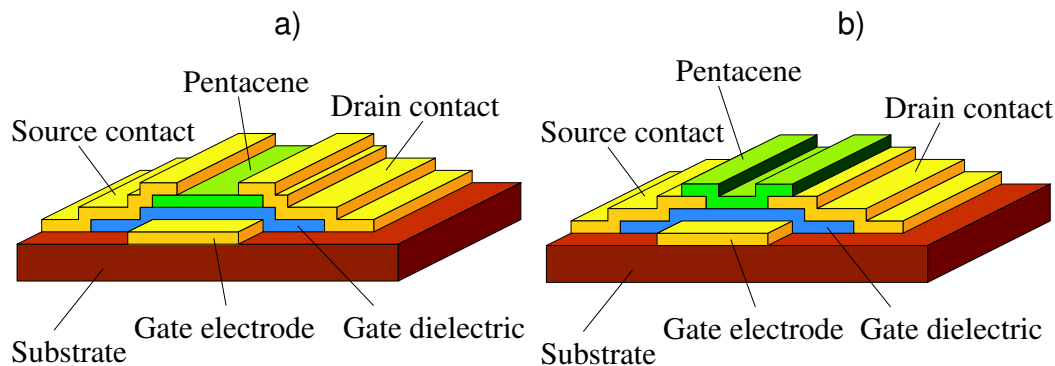


Figure 44: Device structures for Pentacene OFETs for different configuration of the source and drain contacts with respect to the Pentacene layer: a) Top contact design, b) Bottom contact design

intrinsic conductivity is usually low, but can be increased by doping or utilizing a field effect. Pentacene for example is widely used to build OFETs. Often, the structures are fabricated on silicon wafers, using the doped silicon as gate electrode and high quality thermal oxide as gate insulator. Devices with polymeric gate dielectrics are reported in literature [52] and all-plastic transistors built on flexible substrates as well [92, 93]. The structure of such transistors is illustrated in Figure 44 in two configurations, as top contact design and bottom contact design. When they are built on a flexible structure, sensors based on membranes and cantilevers with OFETs as sensing element can be developed. In case Pentacene films exhibit piezoresistive behavior, it could be used in sensor applications with integrated organic electronic circuitry. The same layer as for the sensing part would be the active film for p-type field effect transistors.

Polymer compounds with conductive filler material as piezoresistive thin films are of great interest because they can be applied using the simple processing technologies for solution based materials. Currently, they show advantages over conjugated polymers. The observed gage factors are higher and the stability under ambient conditions is better [70, 71, 72]. Especially sensing devices incorporating carbon nanotubes show a high piezoresistive effect [73, 74, 75]. On the other side, their fabrication is difficult and the control of the precise ratio of ingredients is critical but required to achieve reproducible, high sensitivity.

4.3 General considerations

The use of organic electronics implies several advantages such as low cost for the materials and simple processing like solution based deposition of films. In combination with sensor elements built the same way out of similar substances, the technology will lead to new devices with unique features. The use of flexible substrates will enable access to new fields of applications. The technologies to fabricate devices out of the novel materials are well suited for mass fabrication where screen printing or spray coating will be used. But also for rapid prototyping, novel approaches can be utilized such as direct printing and laser ablation. Together, this will reduce development and fabrication costs and new markets will be accessed with low cost organic electronic devices.

But some drawbacks are inherited from their organic nature as well. Especially the long term stability of devices must be improved. Here, the possibilities of optimizing the chemical structure seems to be limited, simply by the nature of the charge transport mechanism utilized, leading to reactive species. Oxygen and humidity will degrade almost any electro-active organic material. Packaging will play a key role to overcome these obstacles on the way to bring such devices onto the market.

Up to the present, organic electronics do not play an important role in sensor applications or as integrated circuits. Nevertheless, electro-optically active organic materials are successfully used in displays. This is an example that obstacles can be overcome by thorough investigation and engineering work. Very likely, the field of organic electronics will further grow and find many applications, including sensors.

REFERENCES

- [1] B. KLOECK, N. F. DE ROOIJ, “Mechanical sensors,” in *Semiconductor Sensors* (S. M. SZE, ed.), ch. 4, pp. 160–204, New York / Chichester /Brisbane / Toronto / Singapore: John Wiley & Sons, Inc., 1994. 1
- [2] S. D. SENTURIA, *Microsystem Design*, chapter 18.2, pp. 470–474. Boston / Dordrecht / London: Kluwer Academic Publishers, 2001. 1, 1.1.3, 4.2
- [3] A. HIERLEMANN, D. LANGE, C. HAGLEITNER, N. KERNESS, A. KOLL, O. BRAND, H. BALTES, “Application-specific sensor systems based on CMOS chemical microsensors,” *Sensors and Actuators, B: Chemical*, vol. 70, no. 1-3, pp. 2–11, 2000. 1, 1.1.3, 1.4
- [4] C. K. CHIANG, C. R. FINCHER JR., Y. W. PARK, A. J. HEEGER, H. SHIRAKAWA, E. J. LOUIS, S. C. GAU, A. G. MACDIARMID, “Electrical conductivity in doped polyacetylene,” *Physical Review Letters*, vol. 39, no. 17, pp. 1098–1101, 1977. 1.1, 1.2
- [5] A. G. MACDIARMID, “Synthetic metals: A novel role for organic polymers (Nobel lecture),” *Angewandte Chemie International Edition*, vol. 40, no. 14, pp. 2581–2590, 2001. 1.1, 1.1.1, 1.1.2, 1.2
- [6] A. J. HEEGER, “Semiconducting and metallic polymers: The fourth generation of polymeric materials (Nobel lecture),” *Angewandte Chemie International Edition*, vol. 40, no. 14, pp. 2591–2611, 2001. 1.1, 4, 1.2
- [7] H. SHIRAKAWA, “The discovery of polyacetylene film: The dawning of an era of conducting polymers (Nobel lecture),” *Angewandte Chemie International Edition*, vol. 40, no. 14, pp. 2574–2580, 2001. 1.1
- [8] A. AJAYAGHOSH, *Organic Semiconductors*. Lecture notes, Indian Institute of Technology Kanpur, Photosciences and Photonics Division, Regional Research Laboratory, CSIR, 2004. 1, 1.1.2, 4, 6
- [9] F. RODRIGUEZ, C. COHEN, C. OBER, L. A. ARCHER, *Principles of polymer systems*, chapter 1. New York / London: Taylor & Francis, fifth ed., 2003. 1.1.1
- [10] B. KIPPELEN, *ECE8833A, Organic optoelectronics*. Lecture notes, Georgia Institute of Technology, School of Electrical and Computer Engineering, 2004. 1.1.1, 2, 1.2, 3
- [11] H. KANNO, Y. HAMADA, H. TAKAHASHI, “Development of OLED with high stability and luminance efficiency by co-doping methods for full color displays,” *IEEE Journal of Selected Topics in Quantum Electronics*, vol. 10, no. 1, pp. 30–36, 2004. 1.1.1
- [12] S. FORREST, P. BURROWS, M. THOMPSON, “The dawn of organic electronics,” *IEEE Spectrum*, vol. 37, no. 8, pp. 29–34, 2000. 1.1.1
- [13] M. SUZUKI, T. HATAKEYAMA, S. TOKITO, F. SATO, “High-efficiency white phosphorescent polymer light-emitting devices,” *IEEE Journal of selected topics in quantum electronics*, vol. 10, no. 1, pp. 115–120, 2004. 1.1.1

- [14] X. WANG, J. ENGEL, C. LIU, "Liquid crystal polymer (LCP) for MEMS: processes and applications," *Journal of Micromechanics and Microengineering*, vol. 13, no. 5, pp. 628–633, 2003. 1.1.1, 1.4.4
- [15] X. CUI, D. C. MARTIN, "Electrochemical deposition and characterization of poly(3,4-ethylenedioxythiophene) on neural microelectrode arrays," *Sensors and Actuators, B: Chemical*, vol. 89, no. 1-2, pp. 92–102, 2003. 1.1.1
- [16] T. JERANKO, H. TRIBUTSCH, N. S. SARICIFTCI, J. C. HUMMELEN, "Patterns of efficiency and degradation of composite polymer solar cells," *Solar Energy Materials and Solar Cells*, vol. 83, no. 2-3, pp. 247–262, 2004. 1.1.1
- [17] J. C. SCOTT, J. H. KAUFMAN, P. J. BROCK, R. DiPIETRO, J. SALEM, J. A. GOITIA, "Degradation and failure of meh-ppv light-emitting diodes," *Journal of Applied Physics*, vol. 79, no. 5, pp. 2745–2751, 1996. 1.1.1
- [18] P. W. M. BLOM, A. J. M. BERNTSEN, C. T. H. F. LIEDENBAUM, H. F. M. SCHOO, Y. CROONEN, P. VAN DE WEIJER, "Efficiency and stability of polymer light-emitting diodes," *Journal of Materials Science: Materials in Electronics*, vol. 11, no. 2, pp. 105–109, 2000. 1.1.1
- [19] K. YAMASHITA, T. MORI, "Encapsulation of organic light-emitting diode using thermal chemical-vapour-deposition polymer film," *Journal of Physics, D: Applied Physics*, vol. 34, no. 5, pp. 740–743, 2001. 1.1.1
- [20] A. B. CHWANG, M. A. ROTHMAN, S. Y. MAO, R. H. HEWITT, M. S. WEAVER, J. A. SILVERNAIL, K. RAJAN, M. HACK, J. J. BROWN, X. CHU, L. MORO, T. KRAJEWSKI, N. RUTHERFORD, "Thin film encapsulated flexible organic electroluminescent displays," *Applied Physics Letters*, vol. 83, no. 3, pp. 413–415, 2003. 1.1.1
- [21] H. HOFSTRAAT, "Will polymer electronics change the electronics industry?," *First International IEEE Conference on Polymers and Adhesives in Microelectronics and Photonics.*, vol. 121, no. 1-3, pp. 91–94, 2001. (Cat. No.01TH8592). 1.1.1
- [22] J. H. BURROUGHS, D. D. C. BRADLEY, A. R. BROWN, R. N. MARKS, K. MACKAY, R. H. FRIEND, P. L. BURNS, A. B. HOLMES, "Light-emitting diodes based on conjugated polymers," *Letters to Nature*, vol. 347, no. 6293, pp. 539–541, 1990. 1.1.2
- [23] J. A. ROGERS, Z. BAO, A. DODABALAPUR, A. MAKHIJA, "Organic smart pixels and complementary inverter circuits formed on plastic substrates by casting and rubber stamping," *IEEE Electron Device Letters*, vol. 21, no. 3, pp. 100–103, 2000. 1.1.2
- [24] D. HOHNHOLZ, A. G. MACDIARMID, "Line patterning of conducting polymers: new horizons for inexpensive, disposable electronic devices," *Synthetic Metals*, vol. 121, no. 1-3, pp. 1327–1328, 2001. 1.1.2
- [25] W. SEIFERT, H. ALBRECHT, S. MIETKE, T. KÖHLER, M. WERNER, "Processing and electrical characterization of intrinsic conducting polymers for electronic and MEMS application," *Proceedings of SPIE*, vol. 5045, pp. 183–190, 2003. 1.1.2, 3.1
- [26] M. SCHRODNER, S. SENSFUSS, H.-K. ROTH, R.-I. STOHN, W. CLEMENS, A. BERNDT, W. FIX, "Plastic electronics based on semiconducting polymers," *First International IEEE Conference on Polymers and Adhesives in Microelectronics and Photonics.*, pp. 1–8, 2001. (Cat. No.01TH8592). 1.1.2

- [27] G. YU, J. WANG, J. McELVAIN, A. J. HEEGER, "Large-area, full-color image sensor made with semiconducting polymers," *Advanced Materials*, vol. 10, no. 17, pp. 1431–1434, 1998. 1.1.3
- [28] G. MATSUNOBU, Y. OISHI, M. YOKOYAMA, M. HIRAMOTO, "High-speed multiplication-type photodetecting device using organic co-deposited films," *Applied Physics Letters*, vol. 81, no. 7, pp. 1321–1322, 2002. 1.1.3
- [29] S. C. J. MESKERS, J. K. J. VAN DUREN, R. A. J. JANSSEN, F. LOUWET, L. GROENENDAAL, "Infrared detectors with poly(3,4-ethylenedioxythiophene)/poly(styrene sulfonic acid) (PEDOT/PSS) as the active material," *Advanced Materials*, vol. 15, no. 7-8, pp. 613–616, 2003. 1.1.3, 3.4
- [30] S. C. J. MESKERS, J. K. J. VAN DUREN, R. A. J. JANSSEN, "Non-linearity in the i-v characteristic of poly(3,4-ethylenedioxythiophene):poly(styrenesulfonic acid) (PEDOT:PSS) due to joule heating," *Organic Electronics*, vol. 5, no. 4, pp. 207–211, 2004. 1.1.3, 3.4
- [31] A. MICHALSKA, A. GALUSZKIEWICZ, M. OGOŃSKA, M. OCYPA, K. MAKSYMIAK, "PEDOT films: Multifunctional membranes for electrochemical ion sensing," *Journal of Solid State Electrochemistry*, vol. 8, no. 6, pp. 381–389, 2004. 1.1.3
- [32] J. BOBACKA, A. IVASKA, A. LEWENSTAM, "Potentiometric ion sensors based on conducting polymers," *Electroanalysis*, vol. 15, no. 5-6, pp. 366–374, 2003. 1.1.3
- [33] L. DAI, P. SOUNDARRAJAN, T. KIM, "Sensors and sensor arrays based on conjugated polymers and carbon nanotubes," *Pure and Applied Chemistry*, vol. 74, no. 9, pp. 1753–1772, 2002. 1.1.3, 1.4.4
- [34] A. KROS, R. J. M. NOLTE, N. A. J. SOMMERDIJK, "Poly(3,4-ethylenedioxythiophene)-based copolymers for biosensor applications," *Journal of Polymer Science, Part A: Polymer Chemistry*, vol. 40, no. 6, pp. 738–747, 2002. 1.1.3
- [35] J. ENGEL, J. CHEN, Z. FAN, C. LIU, "Polymer micromachined multimodal tactile sensors," *Sensors and Actuators, A: Physical*, vol. 117, no. 1, pp. 50–61, 2004. 1.1.3
- [36] T. SOMEYA, T. SAKURAI, "Integration of organic field effect transistors and rubbery pressure sensors for artificial skin applications," *International Electron Devices Meeting, IEDM, IEEE*, pp. 8.4.1 – 8.4.4, 2003. 1.1.3
- [37] T. JOHANSSON, L. A. A. PETERSSON, O. INGANÄS, "Conductivity of de-doped poly(3,4-ethylenedioxythiophene)," *Synthetic Metals*, vol. 129, no. 3, pp. 269–274, 2002. 1.2, 3.5.3
- [38] Y. PREEZANT, *Electrical properties of contact region of polymeric semiconductor devices*. Master thesis, Technion-Israel Institute of Technology, Department of Electrical Engineering, Mar. 2004. 5, 1.2
- [39] P. W. M. BLOM, M. C. J. M. VISSENBERG, "Charge transport in poly(p-phenylene vinylene) light-emitting diodes," *Materials Science and Engineering, R: Reports*, vol. 27, no. 3-4, pp. 53–94, 2000. 1.2, 8, 1.3.2, 3.5.1
- [40] E.M. CONWELL, "Impurity band conduction in germanium and silicon," *Physical Review*, vol. 103, no. 1, pp. 51–61, 1956. 1.2
- [41] N.F. MOTT, "On the transition to metallic conduction in semiconductors," *Canadian Journal of Physics*, vol. 34, no. 12A, pp. 1356–1368, 1956. 1.2

- [42] A. MILLER, E. ABRAHAMS, "Impurity band conduction in germanium and silicon," *Physical Review*, vol. 120, no. 3, pp. 745–755, 1960. 1.2
- [43] P. M. BORSENBERGER, L. PAUTMEIER, H. BÄSSLER, "Charge transport in disordered molecular solids," *Journal of Chemical Physics*, vol. 94, no. 9, pp. 5447–5454, 1991. 1.2, 3.5.1
- [44] P. M. BORSENBERGER, L. PAUTMEIER, R. RICHERT, H. BÄSSLER, "Hole transport in 1,1-bis(di-4-tolylaminophenyl)cyclohexane," *Journal of Chemical Physics*, vol. 94, no. 12, pp. 8276–8281, 1991. 1.2, 3.5.1
- [45] B. MOVAGHAR, "Transport in polymers," *Philosophical Magazine B*, vol. 65, no. 4, pp. 811–816, 1992. 1.2, 3.5.1
- [46] M. A. ABKOWITZ, "Electronic transport in polymers," *Philosophical Magazine B*, vol. 65, no. 4, pp. 817–829, 1992. 1.2, 3.5.1
- [47] C. TANASE, E. J. MEIJER, P. W. M. BLOM, D. M. LEEUW, "Unification of the hole transport in polymeric field-effect transistors and light-emitting diodes," *Physical Review Letters*, vol. 91, no. 21, p. 216601, 2003. 1.2, 3.5.1
- [48] L. B. SCHEIN, "Comparison of charge transport models in molecularly doped polymers," *Philosophical Magazine B*, vol. 65, no. 4, pp. 795–810, 1992. 1.2, 3.5.1
- [49] M. GRELL, *PHY411 Organic semiconductors and devices*. Lecture notes, University of Sheffield, Department of Physics and Astronomy. 7, 1.3.1, 1.3.2, 9, 1.3.3
- [50] N. KOCH, J. SCHWARTZ, A. KAHN, "Organic molecular films on gold versus conducting polymer: Influence of injection barrier height and morphology on current-voltage characteristics," *Applied Physics Letters*, vol. 82, no. 14, pp. 2281–2283, 2003. 1.3.1
- [51] H. KLAUK, T. N. JACKSON, "Pentacene organic thin-film transistors and ICs," *Solid State Technology*, vol. 43, no. 3, pp. 63–77, 2000. 1.3.1
- [52] J. PUIGDOLLERS, C. VOZ, A. ORPELLA, R. QUIDANT, I. MARTIN, M. VETTER, R. ALCUBILLA, "Pentacene thin-film transistors with polymeric gate dielectric," *Organic Electronics*, vol. 5, no. 1–3, pp. 67–71, 2004. 1.3.1, 4.2
- [53] C. W. TANG, S. A. VAN SLYKE, "Organic electroluminescent diodes," *Applied Physics Letters*, vol. 51, no. 12, pp. 913–915, 1987. 1.3.1
- [54] A. YAMAMORI, C. ADACHI, T. KOYAMA, Y. TANIGUCHI, "Electroluminescence of organic light emitting diodes with a thick hole transport layer composed of a triphenylamine based polymer doped with an antimony compound," *Journal of Applied Physics*, vol. 86, no. 8, pp. 4369–4376, 1999. 1.3.1
- [55] R. W. I. DE BOER, M. E. GERSHENSON, A. F. MORPURGO, V. PODZOROV, "Organic single-crystal field-effect transistors," *Physica Status Solidi (A), Applied Research*, vol. 201, no. 6, pp. 1302–1331, 2004. 1.3.2
- [56] Q. SUN, C. YANG, G. HE, Y. LI, H. WANG, "Effects of electrode modifications on the performance of polymer light-emitting electrochemical cells," *Journal of Polymer Science, B: Polymer Physics*, vol. 33, no. 3, pp. 433–443, 2002. 1.3.2

- [57] L. GROENENDAAL, G. ZOTTI, P.-H. AUBERT, S. M. WAYBRIGHT, J. R. REYNOLDS, "Electrochemistry of poly(3,4-alkylenedioxythiophene) derivatives," *Advanced Materials*, vol. 15, no. 11, pp. 855–879, 2003. 1.3.3, 1.3.3
- [58] D. W. WELSH, A. KUMAR, M. C. MORVANT, J. R. REYNOLDS, "Fast electrochromic polymers based on new poly(3,4-alkylenedioxythiophene) derivatives," *Synthetic Metals*, vol. 102, no. 1-3, pp. 967–968, 1999. 1.3.3
- [59] K. E. AASMUNDTVEIT, E. J. SAMUELSEN, L. A. A. PETTERSSON, O. INGANŠ, T. JOHANSSON, R. FEIDENHANS, "Structure of thin films of poly(3,4-ethylenedioxythiophene)," *Synthetic Metals*, vol. 101, no. 1-3, pp. 561–564, 1999. 1.3.3
- [60] C. W. KWON, G. CAMPET, B. B. KALE, "Structure of thin films of poly(3,4-ethylenedioxythiophene)," *Active and Passive Electronic Components*, vol. 26, no. 2, pp. 81–86, 2003. 1.3.3
- [61] K. BOOK, H. BÄSSLER, A. ELSCHNER, S. KIRCHMEYER, "Hole injection from an ito/pedot anode into the hole transport layer of an OLED probed by bias induced absorption," *Organic Electronics*, vol. 4, no. 4, pp. 227–232, 2003. 1.3.3
- [62] F. CACIALLI, J. S. KIM, T. M. BROWN, J. MORGADO, M. GRANSTRÖM, R. H. FRIEND, G. GIGLI, R. CINGOLANI, L. FAVARETTO, G. BARBARELLA, R. DAIK, W. J. FEAST, "Surface and bulk phenomena in conjugated polymers devices," *Synthetic Metals*, vol. 109, no. 1-3, pp. 7–11, 2000. 1.3.3
- [63] M. C. MORVANT, J. R. REYNOLDS, "In situ conductivity studies of poly(3,4-ethylenedioxythiophene)," *Synthetic Metals*, vol. 92, no. 1, pp. 57–61, 1998. 1.3.3
- [64] J. L. DUVAIL, P. RETHO, C. GODON, C. MARHIC, G. LOUARN, O. CHAUVET, S. CUENOT, B. NYSTEN, L. DAUGINET-DE PRA, S. DEMOUSTIER-CHAMPAGNE, "Physical properties of conducting polymer nanofibers," *Synthetic Metals*, vol. 135-136, pp. 329–330, 2003. 1.3.3
- [65] S. HAFIZOVIC, T. VOLDEN, D. BARRETTINO, K.-U. KIRSTEIN, AND A. HIERLEMANN, "Single-chip atomic force microscope," in *MEMS 2005, Miami*, vol. 18 of *IEEE International Conference on Micro Electro Mechanical Systems*, pp. 638–641, IEEE, 2005. 1.4
- [66] OMEGA, *Force-Related Measurements: Pressure-Strain-Force*, vol. 3 of *Transactions in measurement and control*. Putman Publishing Company and OMEGA Press LLC., 1998. Available online under, <http://www.omega.com/literature/transactions>. 1.4.4, 11, 1.4.4
- [67] R. SCHORNER, "First- and second-order longitudinal piezoresistive coefficients of n-type metal-oxide-semiconductor field-effective transistors," *Journal of Applied Physics*, vol. 67, no. 9, pp. 4354–4357, 1990. 1.4.4
- [68] O. BRAND, *ECE8813B, Theory of microelectromechanical devices*. Lecture notes, Georgia Institute of Technology, School of Electrical and Computer Engineering, 2004. 3, 1.4.4
- [69] K. NODA, K. HOSHINO, K. MATSUMOTO, I. SHIMOYAMA, "300nm thick cantilever in PDMS for tactile sensing," in *MEMS 2005, Miami*, vol. 18 of *IEEE International Conference on Micro Electro Mechanical Systems*, pp. 283–286, IEEE, 2005. 1.4.4
- [70] S. RADHAKRISHNAN, S. CHAKNE, P. N. SHELKE, "High piezoresistivity in conducting polymer composites," in *Materials Letters* (J. H. WERNICK, A. F. W. WILLOUGHBY, ed.), vol. 18 of *Materials Research Society Symposium Proceedings*, pp. 358–362, North-Holland, 1993/1994. 1.4.4, 4.2

- [71] A. B. FRAZIER, M. G. ALLEN, "Piezoresistive graphite/polyimide thin films for micromachining applications," *Journal of Applied Physics*, vol. 73, no. 9, pp. 4428–4433, 1993. 1.4.4, 4.2
- [72] M. KNITE, V. TETERIS, A. KIPLOKA, J. KAUPUZS, "Polyisoprene-carbon black nanocomposites as tensile strain and pressure sensor material," *Sensors and Actuators, A: Physical*, vol. 110, no. 1, pp. 142–149, 2004. 1.4.4, 4.2
- [73] C. K. M. FUNG, M. Q. H. ZHANG, R. H. M. CHAN, W. J. LI, "A PMMA-based micro pressure sensor chip using carbon nanotubes as sensing elements," in *MEMS 2005, Miami*, vol. 18 of *IEEE International Conference on Micro Electro Mechanical Systems*, pp. 251–254, IEEE, 2005. 1.4.4, 4.2
- [74] W.-L. WANG, K.-J. LIAO, Y. LI, Y.-T. WANG, "Piezoresistive effect of doped carbon nanotube/cellulose films," *Chin. Phys. Lett.*, vol. 20, no. 9, pp. 1544–1547, 2003. 1.4.4, 4.2
- [75] W.-L. WANG, K.-J. LIAO, C.-Z. CAI, C.-G. HU, Y. MA, J.-W. LU, "Study on piezoresistivity of doped carbon nanotube films," *Journal of Metastable and Nanocrystalline Materials*, vol. 23, pp. 309–312, 2005. 1.4.4, 4.2
- [76] S. RADHAKRISHNAN, B. K. SWARNENDU, "Effect of dopants ion on piezo-response in polyaniline-poly(vinylidene fluoride) blends," in *Smart Materials II* (A. R. WILSON, V. V. VARADAN, ed.), vol. 4934 of *Proceedings of the International Society for Optical Engineering*, pp. 23–29, SPIE, 2002. 1.4.4
- [77] D. DE ROSSI, A. DELLA SANTA, M. MAZZOLDI, "Piezo- and thermoresistive fabrics for man-machine interfaces," in *Artificial and Natural Perception* (C. DI NATALE, A. D'AMICO, F. DAVIDE, ed.), *Proceedings of the 2nd Italian Conference on Sensors and Microsystems*, pp. 312–316, World Scientific, 1997. 1.4.4
- [78] M. PECHT, X. WU, "Characterization of polyimides used in high density interconnects," *IEEE Transactions on Components, Packaging and Manufacturing Technology, Part B*, vol. 17, no. 4, pp. 632–639, 1994. 2.1, 3.5.2
- [79] DUPONT, "General information about Kapton®." Available online under <http://www.dupont.com>. 2.1, 3.4
- [80] J. EDMAN, D. COULMAN, "The surface and interfacial chemistry of polyimide films," *available from DuPont*, 1996. 2.3
- [81] BAYER, H.C. STARCK, "Baytron® inherently conductive polymer products." Available online under <http://www.hcstarck-chemicals.com>. 4, 3.1
- [82] S. MÖLLER, C. PERLOV, W. JACKSON, C. TAUSSIG, S. R. FORREST, "Electrochromic conductive polymer fuses for hybrid organic/inorganic semiconductor memories," *Journal of Applied Physics*, vol. 94, no. 12, pp. 7811–7819, 2003. 2.4, 3.5.3
- [83] "Sensirion - the sensor company." Information available online under <http://sensirion.com>. 3.2
- [84] "Keithley instruments inc." Information available online under <http://www.keithley.com>. 3.2
- [85] D. NILSSON, T. KUGLER, P. SVENSSON, M. BERGGREN, "An all-organic sensor-transistor based on a novel electrochemical transducer concept printed electrochemical sensor on paper," *Sensors and Actuators, B: Chemical*, vol. 86, no. 2, pp. 193–197, 2002. 3.3

- [86] J. E. MARK, *Physical Properties of Polymers Handbook*, chapter 23.3.6, p. 324. New York: Springer-Verlag, 2001. 3.5.2
- [87] S. MÖLLER, C. PERLOV, W. JACKSON, C. TAUSSIG, S. R. FORREST, “A polymer/semiconductor write-once read-many-times memory,” *Letters to Nature*, vol. 426, no. 6963, pp. 166–169, 2003. 3.5.3
- [88] R. KIEBOOMS, A. ALESHIN, K. HUTCHISON, F. WUDL, A. HEEGER, “Doped poly(3,4-ethylenedioxythiophene) films: thermal, electromagnetical and morphological analysis,” *Synthetic Metals*, vol. 101, no. 1-3, pp. 436–437, 1999. 3.5.3
- [89] H. SIRRINGHAUS, R. J. WILSON, R.H. FRIEND, M. INBASEKARAN, W. WU, E. P. WOO, M. GRELL, D. C. BRADLEY, “Mobility enhancement in conjugated polymer field-effect transistors through chain alignment in a liquid-crystalline phase,” *Applied Physics Letters*, vol. 77, no. 3, pp. 406–408, 2000. 3.6, 4.2
- [90] P. DYREKLEV, G. GUSTAFSSON, O. INGANAS, H. STUBB, “Polymeric field effect transistors using oriented polymers,” *Synthetic Metals*, vol. 57, no. 1, pp. 4093–4098, 1993. 3.6
- [91] J. VAN RUITENBEEK, “Silver nanoswitch,” *Nature*, vol. 433, no. 7021, pp. 21–22, 2005. In this article, the author describes the work done by K. Terabe and co workers. 3.7
- [92] C. J. DRURY, C. M. J. MUTSAERS, C. M. HART, M. MATTERS, D. M. DE LEEUW, “Low-cost all-polymer integrated circuits,” *Applied Physics Letters*, vol. 73, no. 1, pp. 108–110, 1998. 4.2
- [93] E. BRANDON, W. WEST, L. ZHOU, T. JACKSON, G. THERIOT, R. A. B. DEVINE, D. BINKLEY, N. VERMA, R. CRAWFORD, “Flexible electronics for space applications,” in *Flexible Electronics 2004 - Materials and Device Technology* (N. FRUEHAUF, B. R. CHALAMALA, B. E. GNADE, J. JANG, ed.), vol. 814 of *Materials Research Society Symposium Proceedings*, (Warrendale, Pa), pp. 219–230, MRS, Materials Research Society, 2004. 4.2